IRS-Aided SWIPT: Joint Waveform, Active and Passive Beamforming Design Under Nonlinear Harvester Model

Yang Zhao, *Member, IEEE,* Bruno Clerckx, *Senior Member, IEEE,* and Zhenyuan Feng, *Member, IEEE*

***Abstract*—The performance of Simultaneous Wireless Information and Power Transfer (SWIPT) is mainly constrained by the received Radio-Frequency (RF) signal strength. To tackle this problem, we introduce an Intelligent Reflecting Surface (IRS) to compensate the propagation loss and boost the transmission efficiency. This paper proposes a novel IRS-aided SWIPT system where a multi-carrier multi-antenna Access Point (AP) transmits information and power simultaneously, with the assist of an IRS, to a single-antenna User Equipment (UE) employing practical receiving schemes. Considering harvester nonlinearity, we characterize the achievable Rate-Energy (R-E) region through a joint optimization of waveform, active and passive beamforming based on the Channel State Information at the Transmitter (CSIT). This problem is solved by the Block Coordinate Descent (BCD) method, where we obtain the active precoder in closed form, the passive beamforming by the Successive Convex Approximation (SCA) approach, and the waveform amplitude by the Geometric Programming (GP) technique. To facilitate practical implementation, we also propose a low-complexity design based on closed-form adaptive waveform schemes. Simulation results demonstrate the proposed algorithms bring considerable R-E gains with robustness to CSIT inaccuracy and finite IRS states. Results also emphasize the importance of modeling harvester nonlinearity in the passive beamforming and entire IRS-aided SWIPT design.**

***Index Terms*—Simultaneous wireless information and power transfer, intelligent reflecting surface, waveform design, beamforming design, energy harvester nonlinearity.**

I. Introduction

A. Simultaneous Wireless Information and Power Transfer

WITH the great advance in communication performance, a bottleneck of wireless networks has come to energy supply. Simultaneous Wireless Information and Power Transfer (SWIPT) is a promising solution to connect and power mobile devices via Radio-Frequency (RF) waves. It provides low power at μW level but broad coverage up to hundreds of meters in a sustainable and controllable manner, bringing more opportunities to the Internet of Things (IoT) and Machine to Machine (M2M) networks. The upsurge in wireless devices, together with the decrease of electronics power consumption, calls for a re-thinking of future wireless networks based on Wireless Power Transfer (WPT) and SWIPT [1].

The concept of SWIPT was first cast in [2], where the authors investigated the Rate-Energy (R-E) tradeoff for a flat Gaussian channel and typical discrete channels. [3] proposed two practical co-located information and power receivers, i.e., Time Switching (TS) and Power Splitting (PS). Dedicated information and energy beamforming were then investigated in [4], [5] to characterize the R-E region for multi-antenna broadcast and interference channels. On the other hand, [6] pointed out that the RF-to-DC conversion efficiency of rectifiers depends on the input power and waveform shape. It implies that the modeling of the energy harvester, particularly its nonlinearity, has a crucial and significant impact on the waveform preference, resource allocation, and system design of any wireless-powered systems [1], [6], [7]. Motivated by this, [8] derived a tractable nonlinear harvester model based on the Taylor expansion of diode I-V characteristics, then performed joint waveform and beamforming design for WPT. Simulation and experiments showed the benefit of modeling energy harvester nonlinearity in real system design [9], [10] and demonstrated the joint waveform and beamforming strategy as a key technique to expand the operation range [11]. A low-complexity adaptive waveform design by Scaled Matched Filter (SMF) was proposed in [12] to exploit the rectifier nonlinearity, whose advantage is then demonstrated in a prototype with channel acquisition [13]. Beyond WPT, [14] uniquely showed that the rectifier nonlinearity brings radical changes to SWIPT design, namely 1) modulated and unmodulated waveforms are not equally suitable for wireless power delivery, 2) a multi-carrier unmodulated waveform superposed to a multi-carrier modulated waveform can enlarge the R-E region of SWIPT, 3) a combination of PS and TS is generally the best strategy, 4) the optimal input distribution is not the conventional Circularly Symmetric Complex Gaussian (CSCG), 5) the rectifier nonlinearity is beneficial to system performance and is essential to efficient SWIPT design. Those observations, validated experimentally in [9], led to the question: *What is the optimal input distribution for SWIPT under nonlinearity?* This question was answered in [15] for single-carrier SWIPT, and some attempts were further made in [16] for multi-carrier SWIPT. The answer sheds new light to the fundamental limits of SWIPT and practical signaling (e.g., modulation and waveform) strategies. It is now well understood from [14]–[16] that, due to harvester nonlinearity, a combination of CSCG and on-off keying in single-carrier setting and non-zero mean asymmetric inputs in multi-carrier setting lead to significantly larger R-E region compared to conventional CSCG. Recently, [17] used machine learning techniques to design SWIPT signaling under nonlinearity to complement the information-theoretic results of [15], and new modulation

The authors are with the Department of Electrical and Electronic Engineering, Imperial College London, London SW7 2AZ, U.K. (e-mail: {yang.zhao18, b.clerckx, zhenyuan.feng19}@imperial.ac.uk).

This paper has been submitted for publication.

schemes were subsequently invented.

B. Intelligent Reflecting Surface

Intelligent Reflecting Surface (IRS) has recently emerged as a promising technique that adapts the propagation environment to enhance the spectrum and energy efficiency. In practice, an IRS consists of multiple individual sub-wavelength reflecting elements to adjust the amplitude and phase of the incoming signal for a smart reflection (i.e., passive beamforming). Different from the relay, backscatter and Frequency-Selective Surface (FSS) [18], the IRS adaptively assists the primary transmission with passive components to suppress thermal noise but is limited to frequency-dependent reflection.

Inspired by the development of real-time reconfigurable metamaterials [19], the authors of [20] introduced a programmable metasurface that steers or polarizes the electromagnetic wave at a specific frequency to mitigate signal attenuation. Motivated by this, [21] proposed an IRS-assisted Multiple-Input Single-Output (MISO) system and jointly optimized the precoder at the Access Point (AP) and the phase shifts at the IRS to minimize the transmit power. The active and passive beamforming problem was then extended to the discrete phase shift case [22] and the multi-user case [23]. In [24], the authors investigated the impact of non-zero resistance on the reflection pattern and emphasized the dependency of the reflection amplitude on the phase shift for practical IRS. To estimate the cascaded AP-IRS-User Equipment (UE) link without RF-chains at the IRS, practical protocols were developed based on element-wise on/off switching [25], training sequence and reflection pattern design [26], [27], and compressed sensing [28]. The hardware architecture, design challenges and application opportunities of practical IRS are covered in [29]. The authors of [30] considered a novel dynamic passive beamforming for Orthogonal Frequency-Division Multiplexing (OFDM) systems, where the reflection coefficient is varied over consequent time slots to enable flexible resource allocation over time-frequency Resource Blocks (RBs). In [31], a prototype IRS with 256 2-bit elements based on Positive Intrinsic-Negative (PIN) diodes was developed to support real-time high-definition video transmission at GHz and mmWave frequency. Deep reinforcement learning tools were also applied in [32] to assist practical secure beamforming and reflection pattern design under QoS constraints for time-varying channels.

C. IRS-Aided SWIPT

The major issue of WPT and SWIPT is the low harvested DC power, and the passive beamforming provided by the IRS can enhance the end-to-end energy efficiency and boost the harvester input power level. The smart channel control and low power consumption of IRS can bring more opportunities to SWIPT. For multi-user IRS-aided SWIPT systems, dedicated energy beams were proved unnecessary for the Weighted Sum-Power (WSP) maximization problem [33] but essential when fairness issue is considered [34]. It was also claimed that Line-of-Sight (LoS) links could boost the WSP as rank-deficient channels tend to require fewer energy beams [35]. However, [33]–[35] were based on an inaccurate linear energy harvester model that is known in both the RF and the communication literature to be inefficient and inaccurate [1], [6]–[17]. In [36], the authors proposed a scalable resource allocation framework for SWIPT systems involving large-scale IRS, where the reflectors are grouped into tiles and the optimization process is divided into an offline mode-design stage and an online mode-selection stage to reduce overall complexity. It was concluded that the tile-based two-stage algorithm not only enables a flexible balance between performance and complexity but also adapts well to practical IRS and harvester models. A recent tutorial paper [37] provided a comprehensive overview on IRS-aided wireless-powered networks, where channel estimation, resource allocation and practical constraints are discussed in detail. To the best of our knowledge, all existing IRS-aided SWIPT papers considered resource allocation and beamforming design for dedicated information and energy users in a single-carrier network. In this paper, we instead build our design based on a proper nonlinear harvester modeling that captures the dependency of the output DC power on both the power and shape of the input waveform, and marry the benefits of joint multi-carrier waveform and active beamforming optimization for SWIPT with the passive beamforming capability of IRS, to investigate the R-E tradeoff for one SWIPT user with practical co-located information decoder and energy harvester. We ask ourselves the important question: *How to jointly exploit the spatial domain and the frequency domain efficiently through joint waveform and beamforming design to enlarge the R-E region of IRS-aided SWIPT?* The contributions of this paper are summarized as follows.

First, we propose a novel IRS-aided SWIPT architecture based on joint waveform, active and passive beamforming design under the diode nonlinear model proposed in [8]. Although this tractable harvester model accurately reveals how the input power level and waveform shape influence the output DC power, it also introduces design challenges such as frequency compensation (i.e., components of different frequencies compensate and produce DC), waveform coupling (i.e., different waveforms jointly contribute to DC), and high-order objective function. To make an efficient use of the rectifier nonlinearity, we superpose a multi-carrier unmodulated power waveform (deterministic multisine) to a multi-carrier modulated information waveform and evaluate the performance under TS and PS receiving modes. The proposed joint waveform, active and passive beamforming architecture exploits the rectifier nonlinearity, a beamforming gain, and the channel selectivity across spatial and frequency domains to enlarge the achievable R-E region. This is the first paper to propose a joint waveform, active and passive beamforming architecture for IRS-aided SWIPT. By doing so, it is also the first paper to properly model the harvester nonlinearity (including its impact on both power and shape of the incoming waveform) and account for its crucial role in IRS-aided SWIPT.

Second, we characterize each R-E boundary point by energy maximization under rate constraint, and solve the problem by a Block Coordinate Descent (BCD) algorithm based on the Channel State Information at the Transmitter (CSIT). For active beamforming, we prove that the global optimal active information and power precoders coincide at Maximum-Ratio Transmission (MRT) even with rectifier nonlinearity. For passive beamforming, we propose a Successive Convex

Approximation (SCA) algorithm and retrieve the IRS phase shift by eigen decomposition with optimality proof. Finally, the superposed waveform is optimized by the Geometric Programming (GP) technique. The IRS phase shift, active precoder, and waveform amplitude are updated iteratively until convergence. This is the first paper to jointly optimize waveform and active/passive beamforming in IRS-aided SWIPT.

Third, we introduce two closed-form adaptive waveform schemes to avoid the exponential complexity of the GP algorithm. The Water-Filling (WF) strategy for modulated waveform and the SMF strategy for multisine waveform are combined in the time and power domains to facilitate practical SWIPT implementation. To accommodate the suboptimal waveform schemes, we modify the passive beamforming algorithm and characterize the R-E region by varying the duration ratio under TS mode and the combining and splitting ratios under PS mode. The proposed low-complexity designs achieve decent R-E performance in different scenarios.

Fourth, we provide numerical results to evaluate the proposed algorithms. It is concluded that 1) multisine waveform is beneficial to energy transfer especially when the number of subbands is large, 2) TS is preferred at low Signal-to-Noise Ratio (SNR) while PS is preferred at high SNR, 3) there exist two optimal IRS development locations, one close to the AP and one close to the UE, 4) the output SNR scales linearly with the number of transmit antennas and quadratically with the number of IRS elements, 5) due to the rectifier nonlinearity, the output DC current scales quadratically with the number of transmit antennas and quartically with the number of IRS elements, 6) for narrowband SWIPT, the optimal active and passive beamforming for any R-E point are also optimal for the whole R-E region, 7) for broadband SWIPT, the optimal active and passive beamforming depend on specific R-E tradeoff point and require adaptive designs, 8) the proposed algorithms are robust to practical impairments such as inaccurate cascaded CSIT and finite IRS reflection states.

Organization: Section II introduces the system model. Section III formulates the problem and tackles the waveform, active and passive beamforming design. Section IV provides simulation results. Section V concludes the paper.

Notations: Scalars, vectors and matrices are denoted respectively by italic, bold lower-case, and bold upper-case letters. j denotes the imaginary unit. $\mathbf{0}$ and $\mathbf{1}$ denote respectively zero and one vector or matrix. $\boldsymbol{I}$ denotes the identity matrix. $\mathbb{R}_+^{x\times y}$ and $\mathbb{C}^{x\times y}$ denote respectively the subspace spanned by real nonnegative and complex $x\times y$ matrices. $\Re\{\cdot\}$ retrieves the real part of a complex entity. $[\cdot]_{(n)}$ denotes the n-th entry of a vector and $[\cdot]_{(1:n)}$ denotes the first n elements of a vector. $(\cdot)^*$, $(\cdot)^T$, $(\cdot)^H$, $(\cdot)^+$, $|\cdot|$, $\|\cdot\|$ represent respectively the conjugate, transpose, conjugate transpose, ramp function, absolute value, and Euclidean norm. $\arg(\cdot)$, $\mathrm{rank}(\cdot)$, $\mathrm{tr}(\cdot)$, $\mathrm{diag}(\cdot)$ and $\mathrm{diag}^{-1}(\cdot)$ denote respectively the argument, rank, trace, a square matrix with input vector on the main diagonal, and a vector retrieving the main diagonal of the input matrix. $\odot$ denotes the Hadamard product. $\boldsymbol{S}\succeq\mathbf{0}$ means $\boldsymbol{S}$ is positive semi-definite. $\mathbb{A}\{\cdot\}$ extracts the DC component of a signal. $\mathbb{E}_X\{\cdot\}$ takes expectation w.r.t. random variable X (X is omitted for simplicity). The distribution of a CSCG random vector with mean $\mathbf{0}$ and covariance $\boldsymbol{\Sigma}$ is denoted by $\mathcal{CN}(\mathbf{0},\boldsymbol{\Sigma})$. $\sim$ means "distributed as". $(\cdot)^{(i)}$ and $(\cdot)^\star$ denote respectively the i-th iterate and the stationary solution.

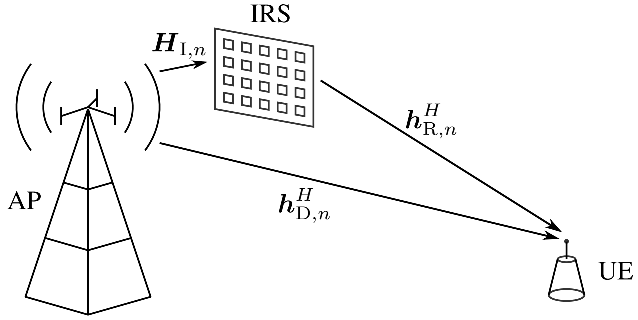

Fig. 1. An IRS-aided multi-carrier SWIPT system.

II. SYSTEM MODEL

As shown in Fig. 1, we propose an IRS-aided SWIPT system where an M-antenna AP delivers information and power simultaneously, through an L-element IRS, to a single-antenna UE over N orthogonal evenly-spaced subbands. We consider the quasi-static block fading model and assume the CSIT of direct and cascaded channels is known. The signals reflected by two or more times are omitted, and the noise power is assumed too small to be harvested.

A. Transmitted Signal

As suggested in [14], we superpose a multi-carrier modulated information-bearing waveform to a multi-carrier unmodulated power-dedicated waveform (deterministic multisine) to boost the spectrum and energy efficiency. The information signal transmitted over subband $n\in\mathcal{N}\triangleq\{1,...,N\}$ at time t is

$$\boldsymbol{x}_{\mathrm{I},n}(t)=\Re\big\{\boldsymbol{w}_{\mathrm{I},n}\tilde{x}_{\mathrm{I},n}(t)e^{j2\pi f_n t}\big\}, \tag{1}$$

where $\boldsymbol{w}_{\mathrm{I},n}\in\mathbb{C}^{M\times 1}$ is the information precoder at subband n, $\tilde{x}_{\mathrm{I},n}\sim\mathcal{CN}(0,1)$ is the information symbol at subband n, and f_n is the frequency of subband n. On the other hand, the power signal transmitted over subband n at time t is

$$\boldsymbol{x}_{\mathrm{P},n}(t)=\Re\big\{\boldsymbol{w}_{\mathrm{P},n}e^{j2\pi f_n t}\big\}, \tag{2}$$

where $\boldsymbol{w}_{\mathrm{P},n}\in\mathbb{C}^{M\times 1}$ is the power precoder at subband n. Therefore, the superposed signal transmitted over all subbands at time t is

$$\boldsymbol{x}(t)=\Re\left\{\sum_{n=1}^{N}(\boldsymbol{w}_{\mathrm{I},n}\tilde{x}_{\mathrm{I},n}(t)+\boldsymbol{w}_{\mathrm{P},n})e^{j2\pi f_n t}\right\}. \tag{3}$$

For simplicity, we define $\boldsymbol{w}_{\mathrm{I/P}}\triangleq[\boldsymbol{w}_{\mathrm{I/P},1}^T,\dots,\boldsymbol{w}_{\mathrm{I/P},N}^T]^T\in\mathbb{C}^{MN\times 1}$.

B. Reflection Pattern and Composite Channel

According to Green's decomposition [38], the backscattered signal of an antenna can be decomposed into the *structural mode* component and the *antenna mode* component. The former is fixed and can be regarded as part of the environment multipath, while the latter is adjustable and depends on the mismatch of the antenna and load impedance. IRS element $l \in \mathcal{L} \triangleq \{1,...,L\}$ varies its impedance $Z_l = R_l + jX_l$ to reflect the incoming signal, and the reflection coefficient is defined as

$$\phi_l = \frac{Z_l - Z_0}{Z_l + Z_0} \triangleq \eta_l e^{j\theta_l}, \tag{4}$$

where Z_0 is the characteristic impedance, $\eta_l \in [0,1]$ is the reflection amplitude[1], and $\theta_l \in [0,2\pi)$ is the phase shift. We also define $\boldsymbol{\phi} \triangleq [\phi_1,...,\phi_L]^H \in \mathbb{C}^{L\times 1}$ and $\boldsymbol{\Theta} \triangleq \mathrm{diag}(\phi_1,...,\phi_L) \in \mathbb{C}^{L\times L}$ as the IRS vector and matrix[2], respectively.

Remark 1. *The element impedance Z_l maps to the reflection coefficient ϕ_l uniquely. Since the reactance X_l depends on the frequency, the reflection coefficient ϕ_l is also a function of frequency and cannot be designed independently at different subbands. In this paper, we assume the bandwidth is small compared to the operating frequency such that the reflection coefficient of each IRS element is the same at all subbands.*

At subband n, we denote the AP-UE direct channel as $\boldsymbol{h}_{\mathrm{D},n}^H \in \mathbb{C}^{1\times M}$, the AP-IRS incident channel as $\boldsymbol{H}_{\mathrm{I},n} \in \mathbb{C}^{L\times M}$, and the IRS-UE reflected channel as $\boldsymbol{h}_{\mathrm{R},n}^H \in \mathbb{C}^{1\times L}$. The auxiliary AP-IRS-UE link can be modeled as a concatenation of the incident channel, the IRS reflection, and the reflected channel. Hence, the composite equivalent channel reduces to

$$\boldsymbol{h}_n^H = \boldsymbol{h}_{\mathrm{D},n}^H + \boldsymbol{h}_{\mathrm{R},n}^H \boldsymbol{\Theta} \boldsymbol{H}_{\mathrm{I},n} = \boldsymbol{h}_{\mathrm{D},n}^H + \boldsymbol{\phi}^H \boldsymbol{V}_n, \tag{5}$$

where we define the cascaded channel without IRS reflection as $\boldsymbol{V}_n \triangleq \mathrm{diag}(\boldsymbol{h}_{\mathrm{R},n}^H)\boldsymbol{H}_{\mathrm{I},n} \in \mathbb{C}^{L\times M}$. For simplicity, we also define $\boldsymbol{h} \triangleq [\boldsymbol{h}_1^T,...,\boldsymbol{h}_N^T]^T \in \mathbb{C}^{MN\times 1}$.

Remark 2. *The cascaded channel varies at different frequencies. Since we regard the reflection as frequency-flat, there exists a tradeoff for the passive beamforming design in the frequency domain. The composite channel can be tuned flexibly to satisfy the specific requirement of the multi-carrier transmission. For example, one can design the reflection pattern to either enhance the strongest subband (e.g., $\max_{\boldsymbol{\phi},n}\|\boldsymbol{h}_n\|$), or improve fairness among subbands (e.g., $\max_{\boldsymbol{\phi}}\min_n\|\boldsymbol{h}_n\|$). This is essentially a resource allocation opportunity at the channel enabled by the IRS. In the MISO case, a similar effect also exists in the spatial domain. Therefore, each reflection coefficient is indeed shared by M antennas over N subbands.*

C. Received Signal

The received superposed signal at the single-antenna UE is[3]

$$y(t) = \Re\left\{\sum_{n=1}^{N} \boldsymbol{h}_n^H (\boldsymbol{w}_{\mathrm{I},n}\tilde{x}_{\mathrm{I},n}(t) + \boldsymbol{w}_{\mathrm{P},n})e^{j2\pi f_n t} + w_n(t)\right\}, \tag{6}$$

where $w_n(t)$ is the noise at RF band n. Note that $y_{\mathrm{I}}(t)$ can be used for energy harvesting if necessary, but $y_{\mathrm{P}}(t)$ carries no information and cannot be used for decoding.

[1]Due to the non-zero power consumption at the IRS, in practice $R_l > 0$ such that $\eta_l < 1$ and is a function of θ_l. This paper sticks to the most common IRS model where the reflection amplitude equals 1 so as to reduce the design complexity and provide a primary benchmark for practical IRS-aided SWIPT.

[2]Note that $\boldsymbol{\phi} = \mathrm{diag}(\boldsymbol{\Phi}^*)$ by definition.

[3]It is assumed that the time difference of signal arrival via direct and auxiliary link is negligible compared to the symbol period.

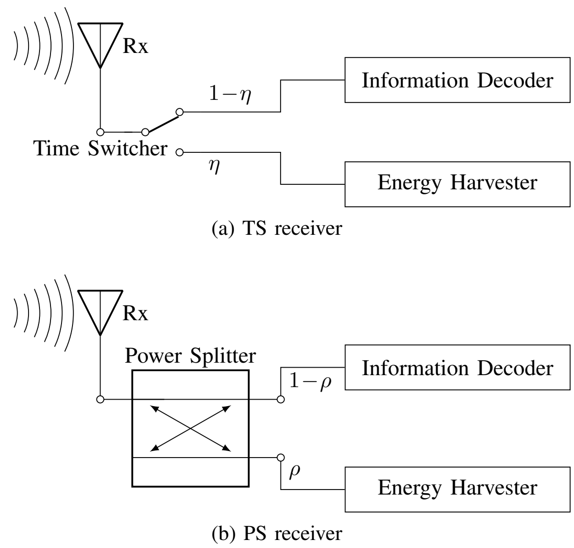

Fig. 2. Practical co-located receiving modes.

D. Receiving Modes

As illustrated in Fig. 2, there are two practical schemes for the co-located information decoder and energy harvester [3] to utilize the superposed signal. The TS receiver divides each transmission block into orthogonal data and energy sessions with duration $1-\eta$ and η, respectively. During each session, the transmitter optimizes the waveform for either Wireless Information Transfer (WIT) or WPT, while the receiver activates the information decoder or the energy harvester correspondingly. Varying η from 0 to 1 characterizes a R-E segment from the WIT point to the WPT point. On the other hand, the PS receiver splits the incoming signal into individual data and energy streams with power ratio $1-\rho$ and ρ, respectively. The data stream is fed into the information decoder while the energy stream is fed into the energy harvester. During each transmission block, the superposed waveform and splitting ratio are jointly designed to achieve different R-E tradeoff. In the following context, we consider the analysis based on the PS receiver since the TS receiver can be regarded as a special case (i.e., a time sharing between $\rho=0$ and $\rho=1$).

E. Information Decoder

A major benefit of the superposed waveform is that the multisine is deterministic and creates no interference to the modulated waveform [14]. Therefore, the achievable rate is[4]

$$R(\boldsymbol{\phi},\boldsymbol{w}_{\mathrm{I}},\rho) = \sum_{n=1}^{N}\log_2\left(1 + \frac{(1-\rho)|\boldsymbol{h}_n^H \boldsymbol{w}_{\mathrm{I},n}|^2}{\sigma_n^2},\right) \tag{7}$$

where σ_n^2 is the variance of the noise at the RF-band and during the RF-to-baseband conversion on tone n.

F. Energy Harvester

Importantly, the rectenna model used in this section taken from [8] captures the dependency of the output DC current

[4]This rate is achievable with waveform cancellation or translated demodulation [14].

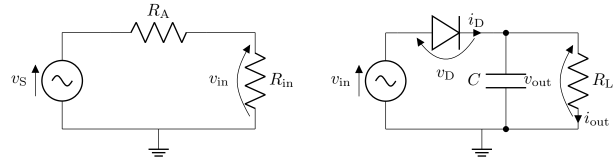

(a) Antenna equivalent circuit (b) A single diode rectifier

Fig. 3. Receive antenna and energy harvester circuits.

on both the power and shape of the received signal. This is critical for efficient signal designs in WPT and SWIPT [39]. Fig. 3(a) illustrates the equivalent circuit of an ideal antenna, where the antenna has an resistance $R_{\rm A}$ and the incoming signal creates an voltage source $v_{\rm S}(t)$. Let $R_{\rm in}$ be the total input resistance of the rectifier and matching network, and we assume the voltage across the matching network is negligible. When perfectly matched (i.e., $R_{\rm in}=R_{\rm A}$), the rectifier input voltage is $v_{\rm in}(t)=y(t)\sqrt{\rho R_{\rm A}}$.

Rectifiers consist of nonlinear components like diode and capacitor to produce DC output and store energy [40]. Consider a simplified rectifier model in Fig. 3(b) where a single series diode is followed by a low-pass filter with a parallel load. As detailed in [8], a truncated Taylor expansion of the diode I-V characteristic equation suggests that, when the subband frequencies are evenly-spaced, maximizing the average output DC current is equivalent to maximizing a monotonic function[5]

$$z(\boldsymbol{\phi},\boldsymbol{w}_{\rm I},\boldsymbol{w}_{\rm P},\rho)=\sum_{i\text{even},i\geq 2}^{n_0} k_i \rho^{i/2} R_{\rm A}^{i/2}\mathbb{E}\big\{\mathbb{A}\big\{y(t)^i\big\}\big\}, \tag{8}$$

where n_0 is the truncation order and $k_i \triangleq i_{\rm S}/i!(n' v_{\rm T})^i$ is the diode coefficient ($i_{\rm S}$ is the reverse bias saturation current, n' is the diode ideality factor, $v_{\rm T}$ is the thermal voltage). With a slight abuse of notation, we refer to z as the average output DC current in this paper. It can be observed that the conventional linear harvester model, where the output DC power equals the sum of the power harvested on each frequency, is a special case of (8) with $n_0=2$. However, due to the coupling effect among different frequencies, some high-order AC components compensate each other and further contribute to the output DC power. In other words, even-order terms with $i\geq 4$ account for the diode nonlinear behavior. For simplicity, we choose $n_0=4$ to investigate the fundamental rectifier nonlinearity, and define $\beta_2 \triangleq k_2 R_{\rm A}$, $\beta_4 \triangleq k_4 R_{\rm A}^2$ to rewrite z by (9). Note that $\mathbb{E}\big\{|\tilde{x}_{{\rm I},n}|^2\big\}=1$ but $\mathbb{E}\big\{|\tilde{x}_{{\rm I},n}|^4\big\}=2$ applies a modulation gain on the nonlinear DC terms. Let $\boldsymbol{W}_{\rm I/P}\triangleq \boldsymbol{w}_{\rm I/P}\boldsymbol{w}_{\rm I/P}^H\in\mathbb{C}^{MN\times MN}$. As illustrated by Fig. 4, $\boldsymbol{W}_{\rm I/P}$ can be divided into $N\times N$ blocks of size $M\times M$, and we let $\boldsymbol{W}_{{\rm I/P},k}$ keep its block diagonal $k\in\mathcal{K}\triangleq\{-N+1,...,N-1\}$ and set all other blocks to $\mathbf{0}$. Hence, the components of z reduce to (10)–(13).

G. Rate-Energy Region

The achievable R-E region is defined as

$$\mathcal{C}_{\rm R-E}\triangleq\Bigg\{(R_{\rm ID},z_{\rm EH})\in\mathbb{R}_+^2 \,|\, R_{\rm ID}\leq R, z_{\rm EH}\leq z,$$

$$\frac{1}{2}\big(\|\boldsymbol{w}_{\rm I}\|^2+\|\boldsymbol{w}_{\rm P}\|^2\big)\leq P\Bigg\}, \tag{14}$$

where P is the average transmit power budget and $1/2$ converts the peak value of sine waves to the average value.

[5]Note that this small-signal expansion model is only valid for the nonlinear operation region of the diode, and the I-V relationship would be linear if the diode behavior is dominated by the load [8].

III. Problem Formulation

We characterize each R-E boundary point through a current maximization problem subject to sum rate, transmit power, and IRS magnitude constraints as

$$\begin{aligned}
\max_{\boldsymbol{\phi},\boldsymbol{w}_{\rm I},\boldsymbol{w}_{\rm P},\rho}\quad & z(\boldsymbol{\phi},\boldsymbol{w}_{\rm I},\boldsymbol{w}_{\rm P},\rho) && \text{(15a)}\\
\text{s.t.}\quad & R(\boldsymbol{\phi},\boldsymbol{w}_{\rm I},\rho)\geq \bar{R}, && \text{(15b)}\\
& \frac{1}{2}\big(\|\boldsymbol{w}_{\rm I}\|^2+\|\boldsymbol{w}_{\rm P}\|^2\big)\leq P, && \text{(15c)}\\
& |\boldsymbol{\phi}|=\mathbf{1}, && \text{(15d)}\\
& 0\leq\rho\leq 1. && \text{(15e)}
\end{aligned}$$

Problem (15) is intricate due to the coupled variables in (15a), (15b) and the non-convex constraint (15d). To obtain a feasible solution, we propose a BCD algorithm that iteratively updates 1) the IRS phase shift, 2) the active precoder, 3) the waveform amplitude and splitting ratio, until convergence.

A. Passive Beamforming

In this section, we optimize the IRS phase shift $\boldsymbol{\phi}$ for any given waveform $\boldsymbol{w}_{\rm I/P}$ and splitting ratio ρ. Note that

$$\begin{aligned}
|\boldsymbol{h}_n^H\boldsymbol{w}_{{\rm I},n}|^2 &= \boldsymbol{w}_{{\rm I},n}^H\boldsymbol{h}_n\boldsymbol{h}_n^H\boldsymbol{w}_{{\rm I},n}\\
&= \boldsymbol{w}_{{\rm I},n}^H(\boldsymbol{h}_{{\rm D},n}+\boldsymbol{V}_n^H\boldsymbol{\phi})(\boldsymbol{h}_{{\rm D},n}^H+\boldsymbol{\phi}^H\boldsymbol{V}_n)\boldsymbol{w}_{{\rm I},n}\\
&= \boldsymbol{w}_{{\rm I},n}^H\boldsymbol{M}_n^H\boldsymbol{\Phi}\boldsymbol{M}_n\boldsymbol{w}_{{\rm I},n}\\
&= \operatorname{tr}(\boldsymbol{M}_n\boldsymbol{w}_{{\rm I},n}\boldsymbol{w}_{{\rm I},n}^H\boldsymbol{M}_n^H\boldsymbol{\Phi})\\
&= \operatorname{tr}(\boldsymbol{C}_n\boldsymbol{\Phi}),
\end{aligned} \tag{16}$$

where $\boldsymbol{M}_n\triangleq[\boldsymbol{V}_n^H,\boldsymbol{h}_{{\rm D},n}]^H\in\mathbb{C}^{(L+1)\times M}$, t' is an auxiliary variable with unit modulus, $\bar{\boldsymbol{\phi}}\triangleq[\boldsymbol{\phi}^H,t']^H\in\mathbb{C}^{(L+1)\times 1}$, $\boldsymbol{\Phi}\triangleq\bar{\boldsymbol{\phi}}\bar{\boldsymbol{\phi}}^H\in\mathbb{C}^{(L+1)\times(L+1)}$, $\boldsymbol{C}_n\triangleq\boldsymbol{M}_n\boldsymbol{w}_{{\rm I},n}\boldsymbol{w}_{{\rm I},n}^H\boldsymbol{M}_n^H\in\mathbb{C}^{(L+1)\times(L+1)}$. On the other hand, we define $t_{{\rm I/P},k}$ as

$$\begin{aligned}
t_{{\rm I/P},k} &\triangleq \boldsymbol{h}^H\boldsymbol{W}_{{\rm I/P},k}\boldsymbol{h}\\
&= \operatorname{tr}(\boldsymbol{h}\boldsymbol{h}^H\boldsymbol{W}_{{\rm I/P},k})\\
&= \operatorname{tr}\Big((\boldsymbol{h}_D+\boldsymbol{V}^H\boldsymbol{\phi})(\boldsymbol{h}_D^H+\boldsymbol{\phi}^H\boldsymbol{V})\boldsymbol{W}_{{\rm I/P},k}\Big)\\
&= \operatorname{tr}(\boldsymbol{M}^H\boldsymbol{\Phi}\boldsymbol{M}\boldsymbol{W}_{{\rm I/P},k})\\
&= \operatorname{tr}(\boldsymbol{M}\boldsymbol{W}_{{\rm I/P},k}\boldsymbol{M}^H\boldsymbol{\Phi})\\
&= \operatorname{tr}(\boldsymbol{C}_{{\rm I/P},k}\boldsymbol{\Phi}),
\end{aligned} \tag{17}$$

where $\boldsymbol{V}\triangleq[\boldsymbol{V}_1,\ldots,\boldsymbol{V}_N]\in\mathbb{C}^{L\times MN}$, $\boldsymbol{M}\triangleq[\boldsymbol{V}^H,\boldsymbol{h}_D]^H\in\mathbb{C}^{(L+1)\times MN}$, $\boldsymbol{C}_{{\rm I/P},k}\triangleq\boldsymbol{M}\boldsymbol{W}_{{\rm I/P},k}\boldsymbol{M}^H\in\mathbb{C}^{(L+1)\times(L+1)}$. On

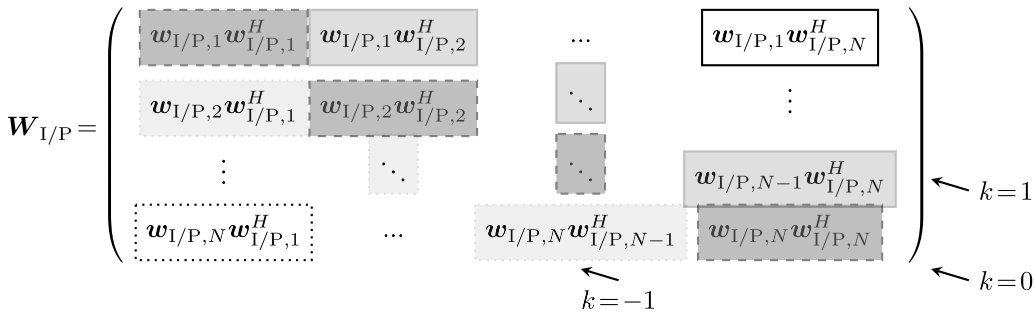

Fig. 4. $\boldsymbol{W}_{\mathrm{I/P}}$ consists of $N\times N$ blocks of size $M\times M$. $\boldsymbol{W}_{\mathrm{I/P},k}$ keeps the k-th block diagonal of $\boldsymbol{W}_{\mathrm{I/P}}$ and nulls all remaining blocks. Solid, dashed and dotted blocks correspond to $k>0$, $k=0$ and $k<0$, respectively. For $\boldsymbol{w}_{\mathrm{I/P},n_1}\boldsymbol{w}^H_{\mathrm{I/P},n_2}$, the k-th block diagonal satisfies $k=n_2-n_1$.

top of this, (7) and (9) reduce respectively to

$$R(\boldsymbol{\Phi})=\sum_{n=1}^{N}\log_2\left(1+\frac{(1-\rho)\mathrm{tr}(\boldsymbol{C}_n\boldsymbol{\Phi})}{\sigma_n^2}\right), \tag{18}$$

$$\begin{aligned} z(\boldsymbol{\Phi})=&\frac{1}{2}\beta_2\rho(t_{\mathrm{I},0}+t_{\mathrm{P},0})\\ &+\frac{3}{8}\beta_4\rho^2\left(2t_{\mathrm{I},0}^2+\sum_{k=-N+1}^{N-1}t_{\mathrm{P},k}t_{\mathrm{P},k}^*\right)\\ &+\frac{3}{2}\beta_4\rho^2 t_{\mathrm{I},0}t_{\mathrm{P},0}. \end{aligned} \tag{19}$$

To maximize the non-concave expression (19), we successively lower bound the second-order terms by their first-order Taylor expansions [41]. Based on the solution at iteration $i-1$, the approximations at iteration i are

$$(t_{\mathrm{I},0}^{(i)})^2\geq 2t_{\mathrm{I},0}^{(i)}t_{\mathrm{I},0}^{(i-1)}-(t_{\mathrm{I},0}^{(i-1)})^2, \tag{20}$$

$$t_{\mathrm{P},k}^{(i)}(t_{\mathrm{P},k}^{(i)})^*\geq 2\Re\left\{t_{\mathrm{P},k}^{(i)}(t_{\mathrm{P},k}^{(i-1)})^*\right\}-t_{\mathrm{P},k}^{(i-1)}(t_{\mathrm{P},k}^{(i-1)})^*, \tag{21}$$

$$t_{\mathrm{I},0}^{(i)}t_{\mathrm{P},0}^{(i)}\geq t_{\mathrm{I},0}^{(i)}t_{\mathrm{P},0}^{(i-1)}+t_{\mathrm{P},0}^{(i)}t_{\mathrm{I},0}^{(i-1)}-t_{\mathrm{I},0}^{(i-1)}t_{\mathrm{P},0}^{(i-1)}. \tag{22}$$

Note that $t_{\mathrm{I/P},0}=\mathrm{tr}(\boldsymbol{C}_{\mathrm{I/P},0}\boldsymbol{\Phi})$ is real because $\boldsymbol{C}_{\mathrm{I/P},0}$ and $\boldsymbol{\Phi}$ are Hermitian matrices. Due to symmetry [42], we have

$$\sum_{k=-N+1}^{N-1}\Re\left\{t_{\mathrm{P},k}^{(i)}(t_{\mathrm{P},k}^{(i-1)})^*\right\}=\sum_{k=-N+1}^{N-1}t_{\mathrm{P},k}^{(i)}(t_{\mathrm{P},k}^{(i-1)})^*. \tag{23}$$

Plugging (20)–(23) into (19), we obtain the DC current approximation $\tilde{z}$ as (24) and transform problem (15) to

$$\begin{aligned} \max_{\boldsymbol{\Phi}}\quad & \tilde{z}(\boldsymbol{\Phi}) && \text{(25a)}\\ \text{s.t.}\quad & R(\boldsymbol{\Phi})\geq\bar{R}, && \text{(25b)}\\ & \mathrm{diag}^{-1}(\boldsymbol{\Phi})=\boldsymbol{1}, && \text{(25c)}\\ & \boldsymbol{\Phi}\succeq\boldsymbol{0}, && \text{(25d)}\\ & \mathrm{rank}(\boldsymbol{\Phi})=1. && \text{(25e)} \end{aligned}$$

We then apply Semi-Definite Relaxation (SDR) to the unit-rank constraint (25e) and formulate a Semi-Definite Programming (SDP) with approximation accuracy no greater than $\pi/4$ [43]. In this specific case, we found the solution provided by CVX toolbox [44] to (25a)-(25d) is always rank-1. This conclusion is summarized below.

Proposition 1. *Any optimal solution $\boldsymbol{\Phi}^\star$ to the relaxed passive beamforming problem* (25a)–(25d) *is rank-*1 *such that* (25e) *is tight and no loss is introduced by SDR.*

Proof. Please refer to Appendix A. □

In summary, we update $\boldsymbol{\Phi}^{(i)}$ until convergence, extract $\hat{\boldsymbol{\phi}}^\star$ by eigen decomposition, and retrieve the IRS vector by $\boldsymbol{\phi}^\star=e^{j\arg\left([\hat{\boldsymbol{\phi}}^\star]_{(1:L)}/[\hat{\boldsymbol{\phi}}^\star]_{(L+1)}\right)}$. The passive beamforming design is summarized in the SCA Algorithm 1, where the relaxed problem (25a)–(25d) involves a $(L+1)$-order positive

$$z(\boldsymbol{\phi},\boldsymbol{w}_{\mathrm{I}},\boldsymbol{w}_{\mathrm{P}},\rho)=\beta_2\rho\Big(\mathbb{E}\big\{\mathbb{A}\{y_{\mathrm{I}}^2(t)\}\big\}+\mathbb{A}\big\{y_{\mathrm{P}}^2(t)\big\}\Big)+\beta_4\rho^2\Big(\mathbb{E}\big\{\mathbb{A}\{y_{\mathrm{I}}^4(t)\}\big\}+\mathbb{A}\big\{y_{\mathrm{P}}^4(t)\big\}+6\mathbb{E}\big\{\mathbb{A}\{y_{\mathrm{I}}^2(t)\}\big\}\mathbb{A}\big\{y_{\mathrm{P}}^2(t)\big\}\Big), \tag{9}$$

$$\mathbb{E}\big\{\mathbb{A}\{y_{\mathrm{I}}^2(t)\}\big\}=\frac{1}{2}\sum_{n=1}^{N}(\boldsymbol{h}_n^H\boldsymbol{w}_{\mathrm{I},n})(\boldsymbol{h}_n^H\boldsymbol{w}_{\mathrm{I},n})^*=\frac{1}{2}\boldsymbol{h}^H\boldsymbol{W}_{\mathrm{I},0}\boldsymbol{h}, \tag{10}$$

$$\mathbb{E}\big\{\mathbb{A}\{y_{\mathrm{I}}^4(t)\}\big\}=\frac{3}{4}\left(\sum_{n=1}^{N}(\boldsymbol{h}_n^H\boldsymbol{w}_{\mathrm{I},n})(\boldsymbol{h}_n^H\boldsymbol{w}_{\mathrm{I},n})^*\right)^2=\frac{3}{4}(\boldsymbol{h}^H\boldsymbol{W}_{\mathrm{I},0}\boldsymbol{h})^2, \tag{11}$$

$$\mathbb{A}\big\{y_{\mathrm{P}}^2(t)\big\}=\frac{1}{2}\sum_{n=1}^{N}(\boldsymbol{h}_n^H\boldsymbol{w}_{\mathrm{P},n})(\boldsymbol{h}_n^H\boldsymbol{w}_{\mathrm{P},n})^*=\frac{1}{2}\boldsymbol{h}^H\boldsymbol{W}_{\mathrm{P},0}\boldsymbol{h}, \tag{12}$$

$$\mathbb{A}\big\{y_{\mathrm{P}}^4(t)\big\}=\frac{3}{8}\sum_{\substack{n_1,n_2,n_3,n_4\\ n_1+n_2=n_3+n_4}}(\boldsymbol{h}_{n_1}^H\boldsymbol{w}_{\mathrm{P},n_1})(\boldsymbol{h}_{n_2}^H\boldsymbol{w}_{\mathrm{P},n_2})(\boldsymbol{h}_{n_3}^H\boldsymbol{w}_{\mathrm{P},n_3})^*(\boldsymbol{h}_{n_4}^H\boldsymbol{w}_{\mathrm{P},n_4})^*=\frac{3}{8}\sum_{k=-N+1}^{N-1}(\boldsymbol{h}^H\boldsymbol{W}_{\mathrm{P},k}\boldsymbol{h})(\boldsymbol{h}^H\boldsymbol{W}_{\mathrm{P},k}\boldsymbol{h})^*. \tag{13}$$

Algorithm 1 SCA: IRS Phase Shift.

Input β_2, β_4, $\boldsymbol{h}_{\mathrm{D},n}$, $\boldsymbol{V}_n$, σ_n, $\boldsymbol{w}_{\mathrm{I/P},n}$, ρ, $\bar{R}$, ϵ, $\forall n$
Construct $\boldsymbol{V}$, $\boldsymbol{M}$, $\boldsymbol{M}_n$, $\boldsymbol{C}_n$, $\boldsymbol{C}_{\mathrm{I/P},k}$, $\forall n,k$
Initialize $i \leftarrow 0$, $\boldsymbol{\Phi}^{(0)}$
Set $t_{\mathrm{I/P},k}^{(0)}$, $\forall k$ by (17)
Compute $z^{(0)}$ by (19)
Repeat
    $i \leftarrow i+1$
    Get $\boldsymbol{\Phi}^{(i)}$ by solving (25a)–(25d)
    Update $t_{\mathrm{I/P},k}^{(i)}$, $\forall k$ by (17)
    Compute $z^{(i)}$ by (19)
Until $|z^{(i)} - z^{(i-1)}| \leq \epsilon$
Set $\boldsymbol{\Phi}^{\star} = \boldsymbol{\Phi}^{(i)}$
Get $\hat{\boldsymbol{\phi}}^{\star}$ by eigen decomposition, $\boldsymbol{\Phi}^{\star} = \hat{\boldsymbol{\phi}}^{\star} (\hat{\boldsymbol{\phi}}^{\star})^H$
Set $\boldsymbol{\phi}^{\star} = e^{j\arg\left([\hat{\boldsymbol{\phi}}^{\star}]_{(1:L)} / [\hat{\boldsymbol{\phi}}^{\star}]_{(L+1)}\right)}$
Output $\boldsymbol{\phi}^{\star}$

semi-definite matrix variable and $(L+2)$ linear constraints. Given a solution accuracy ϵ_{IPM} for the interior-point method, the computational complexity of Algorithm 1 is $\mathcal{O}\left(I_{\mathrm{SCA}}(L+2)^4(L+1)^{0.5}\log(\epsilon_{\mathrm{IPM}}^{-1})\right)$, where I_{SCA} denotes the number of SCA iterations [43].

Proposition 2. *For any feasible initial point with given waveform and splitting ratio, the SCA Algorithm 1 is guaranteed to converge to local optimal points of the original problem* (15).

Proof. Please refer to Appendix B. □

B. Active Beamforming

To avoid straightforward optimization over complex vectors $\boldsymbol{w}_{\mathrm{I/P}}$ of size $MN \times 1$, we decouple the waveform in the spatial and frequency domains to reduce the size of variables. The weight on subband n is essentially

$$\boldsymbol{w}_{\mathrm{I/P},n} = s_{\mathrm{I/P},n} \boldsymbol{b}_{\mathrm{I/P},n}, \tag{26}$$

where $s_{\mathrm{I/P},n}$ denotes the amplitude of the modulated/multisine waveform at tone n, and $\boldsymbol{b}_{\mathrm{I/P},n}$ denotes the corresponding information/power precoder. Define $\boldsymbol{s}_{\mathrm{I/P}} \triangleq [s_{\mathrm{I/P},1}, \ldots, s_{\mathrm{I/P},N}]^T \in \mathbb{R}_+^{N\times 1}$. The MRT precoder at subband n is given by

$$\boldsymbol{b}_{\mathrm{I/P},n}^{\star} = \frac{\boldsymbol{h}_n}{\|\boldsymbol{h}_n\|}. \tag{27}$$

Proposition 3. *For single-user SWIPT, the global optimal information and power precoders coincide at the MRT.*

Proof. Please refer to Appendix C. □

C. Waveform and Splitting Ratio

Next, we jointly optimize the waveform amplitude $\boldsymbol{s}_{\mathrm{I/P}}$ and the splitting ratio ρ for any given IRS phase shift $\boldsymbol{\phi}$ and active precoder $\boldsymbol{b}_{\mathrm{I/P},n}$, $\forall n$. On top of (27), the equivalent channel strength at subband n is $\|\boldsymbol{h}_n\|$ and the rate (7) reduces to

$$R(\boldsymbol{s}_{\mathrm{I}}, \rho) = \log_2 \prod_{n=1}^{N} \left(1 + \frac{(1-\rho)\|\boldsymbol{h}_n\|^2 s_{\mathrm{I},n}^2}{\sigma_n^2}\right), \tag{28}$$

and the DC current (9) rewrites as (29), so that problem (15) boils down to

$$\max_{\boldsymbol{s}_{\mathrm{I}}, \boldsymbol{s}_{\mathrm{P}}, \rho} \quad z(\boldsymbol{s}_{\mathrm{I}}, \boldsymbol{s}_{\mathrm{P}}, \rho) \tag{30a}$$
$$\text{s.t.} \quad R(\boldsymbol{s}_{\mathrm{I}}, \rho) \geq \bar{R}, \tag{30b}$$
$$\frac{1}{2}\left(\|\boldsymbol{s}_{\mathrm{I}}\|^2 + \|\boldsymbol{s}_{\mathrm{P}}\|^2\right) \leq P. \tag{30c}$$

Following [14], we introduce auxiliary variables $t'', \bar{\rho}$[6] and transform problem (30) into a reversed GP

$$\min_{\boldsymbol{s}_{\mathrm{I}}, \boldsymbol{s}_{\mathrm{P}}, \rho, \bar{\rho}, t''} \quad \frac{1}{t''} \tag{31a}$$
$$\text{s.t.} \quad \frac{t''}{z(\boldsymbol{s}_{\mathrm{I}}, \boldsymbol{s}_{\mathrm{P}}, \rho)} \leq 1, \tag{31b}$$
$$\frac{2^{\bar{R}}}{\prod_{n=1}^{N}\left(1 + \bar{\rho}\|\boldsymbol{h}_n\|^2 s_{\mathrm{I},n}^2 / \sigma_n^2\right)} \leq 1, \tag{31c}$$
$$\frac{1}{2}\left(\|\boldsymbol{s}_{\mathrm{I}}\|^2 + \|\boldsymbol{s}_{\mathrm{P}}\|^2\right) \leq P, \tag{31d}$$
$$\rho + \bar{\rho} \leq 1. \tag{31e}$$

The denominators of (31c) and (31b) consist of posynomials [45] that can be decomposed as sums of monomials

$$1 + \frac{\bar{\rho}\|\boldsymbol{h}_n\|^2 s_{\mathrm{I},n}^2}{\sigma_n^2} \triangleq \sum_{m_{\mathrm{I},n}} g_{m_{\mathrm{I},n}}(s_{\mathrm{I},n}, \bar{\rho}), \tag{32}$$

$$z(\boldsymbol{s}_{\mathrm{I}}, \boldsymbol{s}_{\mathrm{P}}, \rho) \triangleq \sum_{m_{\mathrm{P}}} g_{m_{\mathrm{P}}}(\boldsymbol{s}_{\mathrm{I}}, \boldsymbol{s}_{\mathrm{P}}, \rho), \tag{33}$$

where $m_{\mathrm{I},n} = 2$ and $m_{\mathrm{P}} = (2N^3 + 6N^2 + 7N)/3$. We upper bound (32) and (33) by the Arithmetic Mean-Geometric Mean (AM-GM) inequality [46] and transform problem (31) to

$$\min_{\boldsymbol{s}_{\mathrm{I}}, \boldsymbol{s}_{\mathrm{P}}, \rho, \bar{\rho}, t''} \quad \frac{1}{t''} \tag{34a}$$
$$\text{s.t.} \quad t'' \prod_{m_{\mathrm{P}}} \left(\frac{g_{m_{\mathrm{P}}}(\boldsymbol{s}_{\mathrm{I}}, \boldsymbol{s}_{\mathrm{P}}, \rho)}{\gamma_{m_{\mathrm{P}}}}\right)^{-\gamma_{m_{\mathrm{P}}}} \leq 1, \tag{34b}$$
$$2^{\bar{R}} \prod_{n} \prod_{m_{\mathrm{I},n}} \left(\frac{g_{m_{\mathrm{I},n}}(s_{\mathrm{I},n}, \bar{\rho})}{\gamma_{m_{\mathrm{I},n}}}\right)^{-\gamma_{m_{\mathrm{I},n}}} \leq 1, \tag{34c}$$

[6] It can be concluded $\bar{\rho}^{\star} = 1 - \rho^{\star}$ because the R-E tradeoff is maximized when no signal component is wasted at the receiver.

$$\tilde{z}(\boldsymbol{\Phi}^{(i)}) = \frac{1}{2}\beta_2\rho(t_{\mathrm{I},0}^{(i)} + t_{\mathrm{P},0}^{(i)}) + \frac{3}{8}\beta_4\rho^2\left(4t_{\mathrm{I},0}^{(i)}t_{\mathrm{I},0}^{(i-1)} - 2(t_{\mathrm{I},0}^{(i-1)})^2 + \sum_{k=-N+1}^{N-1} 2t_{\mathrm{P},k}^{(i)}(t_{\mathrm{P},k}^{(i-1)})^* - t_{\mathrm{P},k}^{(i-1)}(t_{\mathrm{P},k}^{(i-1)})^*\right)$$
$$+ \frac{3}{2}\beta_4\rho^2\left(t_{\mathrm{I},0}^{(i)}t_{\mathrm{P},0}^{(i-1)} + t_{\mathrm{P},0}^{(i)}t_{\mathrm{I},0}^{(i-1)} - t_{\mathrm{I},0}^{(i-1)}t_{\mathrm{P},0}^{(i-1)}\right). \tag{24}$$

Algorithm 2 GP: Waveform Amplitude and Splitting Ratio.

Input β_2, β_4, $\boldsymbol{h}_n$, P, σ_n, $\bar{R}$, ϵ, $\forall n$
Initialize $i \leftarrow 0$, $\boldsymbol{s}_{\mathrm{I/P}}^{(0)}$, $\rho^{(0)}$
Compute $R^{(0)}$, $z^{(0)}$ by (28), (29)
Set $g_{m_{\mathrm{I},n}}^{(0)}$, $g_{m_{\mathrm{P}}}^{(0)}$, $\forall n$ by (32), (33)
Repeat
  $i \leftarrow i+1$
  Update $\gamma_{m_{\mathrm{I},n}}^{(i)}$, $\gamma_{m_{\mathrm{P}}}^{(i)}$, $\forall n$ by (35), (36)
  Get $\boldsymbol{s}_{\mathrm{I/P}}^{(i)}$, $\rho^{(i)}$ by solving problem (34)
  Compute $R^{(i)}$, $z^{(i)}$ by (28), (29)
  Update $g_{m_{\mathrm{I},n}}^{(i)}$, $g_{m_{\mathrm{P}}}^{(i)}$, $\forall n$ by (32), (33)
Until $|z^{(i)} - z^{(i-1)}| \leq \epsilon$
Set $\boldsymbol{s}_{\mathrm{I/P}}^{\star} = \boldsymbol{s}_{\mathrm{I/P}}^{(i)}$, $\rho^{\star} = \rho^{(i)}$
Output $\boldsymbol{s}_{\mathrm{I}}^{\star}$, $\boldsymbol{s}_{\mathrm{P}}^{\star}$, $\rho^{\star}$

$$\frac{1}{2}\left(\|\boldsymbol{s}_{\mathrm{I}}\|^2 + \|\boldsymbol{s}_{\mathrm{P}}\|^2\right) \leq P, \tag{34d}$$

$$\rho + \bar{\rho} \leq 1, \tag{34e}$$

where $\gamma_{m_{\mathrm{I},n}} \geq 0$, $\gamma_{m_{\mathrm{P}}} \geq 0$, $\sum_{m_{\mathrm{I},n}} \gamma_{m_{\mathrm{I},n}} = \sum_{m_{\mathrm{P}}} \gamma_{m_{\mathrm{P}}} = 1$. The tightness of the AM-GM inequality depends on $\{\gamma_{m_{\mathrm{I},n}}, \gamma_{m_{\mathrm{P}}}\}$, and a feasible choice at iteration i is

$$\gamma_{m_{\mathrm{I},n}}^{(i)} = \frac{g_{m_{\mathrm{I},n}}(s_{\mathrm{I},n}^{(i-1)}, \bar{\rho}^{(i-1)})}{1 + \bar{\rho}^{(i-1)} \|\boldsymbol{h}_n\|^2 (s_{\mathrm{I},n}^{(i-1)})^2 / \sigma_n^2}, \tag{35}$$

$$\gamma_{m_{\mathrm{P}}}^{(i)} = \frac{g_{m_{\mathrm{P}}}(\boldsymbol{s}_{\mathrm{I}}^{(i-1)}, \boldsymbol{s}_{\mathrm{P}}^{(i-1)}, \rho^{(i-1)})}{z(\boldsymbol{s}_{\mathrm{I}}^{(i-1)}, \boldsymbol{s}_{\mathrm{P}}^{(i-1)}, \rho^{(i-1)})}. \tag{36}$$

With (35) and (36), problem (34) can be solved by existing optimization tools such as CVX [44]. We update $\boldsymbol{s}_{\mathrm{I}}^{(i)}, \boldsymbol{s}_{\mathrm{P}}^{(i)}, \rho^{(i)}$ iteratively until convergence. The joint waveform amplitude and splitting ratio design is summarized in the GP Algorithm 2, which achieves local optimality at the cost of exponential computational complexity [46].

Proposition 4. *For any feasible initial point, the GP Algorithm 2 is guaranteed to converge to local optimal points of the waveform amplitude and splitting ratio design problem* (30).

Proof. Please refer to [8], [14]. □

D. Low-Complexity Adaptive Design

To facilitate practical SWIPT implementation, we propose two closed-form adaptive waveform amplitude schemes by combining WF and SMF in the time and power domains. For WIT, the optimal WF strategy assigns the amplitude of modulated tone n by

$$s_{\mathrm{I},n} = \sqrt{2\left(\lambda - \frac{\sigma_n^2}{P\|\boldsymbol{h}_n\|^2}\right)^+}, \tag{37}$$

where λ is chosen to satisfy the power constraint $\|\boldsymbol{s}_I\|^2/2 \leq P$. The closed-form solution can be obtained by iterative power allocation [47], and the details are omitted here. On the other hand, SMF was proposed in [12] as a suboptimal WPT resource allocation scheme that assigns the amplitude of sinewave n by

$$s_{\mathrm{P},n} = \sqrt{\frac{2P}{\sum_{n=1}^{N} \|\boldsymbol{h}_n\|^{2\alpha}}} \|\boldsymbol{h}_n\|^{\alpha}, \tag{38}$$

where the scaling ratio $\alpha \geq 1$ is given and can be adjusted to exploit the rectifier nonlinearity and frequency selectivity. When the receiver works in TS mode, there is no superposition in the suboptimal waveform design. Modulated waveform with amplitude (37) is used in the data session while multisine waveform with amplitude (38) is used in the energy session. When the receiver works in PS mode, we jointly design the combining ratio δ with the splitting ratio ρ, and assign the superposed waveform amplitudes as

$$s_{\mathrm{I},n} = \sqrt{2(1-\delta)\left(\lambda - \frac{\sigma_n^2}{P\|\boldsymbol{h}_n\|^2}\right)^+}, \tag{39}$$

$$s_{\mathrm{P},n} = \sqrt{\frac{2\delta P}{\sum_{n=1}^{N} \|\boldsymbol{h}_n\|^{2\alpha}}} \|\boldsymbol{h}_n\|^{\alpha}, \tag{40}$$

where the combining ratio δ determines the weight on multisine power waveform at the transmitter and the splitting ratio ρ determines the priority of the energy harvester at the receiver[7]. Besides, minor modifications are required for passive beamforming to accommodate both low-complexity waveform schemes. To achieve the WIT point, the rate (18) instead of the DC current (24) should be maximized. In such case, the current expression is dropped and no SCA is involved. To achieve any non-WIT point (i.e., $z \neq 0$), the rate constraint (25b) should be dropped as the achievable rate depends on either η or $\{\delta, \rho\}$. The Modified-SCA (M-SCA) Algorithm 3 summarizes the modified passive beamforming design when the receiver works in PS mode. The proofs of SDR tightness and local optimality are similar to Appendices A and B thus omitted here. Compared with Algorithm 1, the rate constraint (25b) is dropped and each SDP in Algorithm 3 involves $(L+1)$ linear

[7] We notice that $\delta^{\star} = \rho^{\star} = 0$ at the WIT point and $\delta^{\star} = \rho^{\star} = 1$ at the WPT point. Heuristically, $\delta^{\star}$ and $\rho^{\star}$ should approximately equal at each point to boost R-E tradeoff.

$$z(\boldsymbol{s}_{\mathrm{I}}, \boldsymbol{s}_{\mathrm{P}}, \rho) = \frac{1}{2}\beta_2 \rho \sum_{n=1}^{N} \|\boldsymbol{h}_n\|^2 (s_{\mathrm{I},n}^2 + s_{\mathrm{P},n}^2) + \frac{3}{8}\beta_4 \rho^2 \left(2 \sum_{n_1, n_2} \prod_{j=1}^{2} \|\boldsymbol{h}_{n_j}\|^2 s_{\mathrm{I},n_j}^2 + \sum_{\substack{n_1, n_2, n_3, n_4 \\ n_1 + n_2 = n_3 + n_4}} \prod_{j=1}^{4} \|\boldsymbol{h}_{n_j}\| s_{\mathrm{P},n_j} \right)$$
$$+ \frac{3}{2}\beta_4 \rho^2 \left(\sum_{n_1, n_2} \|\boldsymbol{h}_{n_1}\|^2 \|\boldsymbol{h}_{n_2}\|^2 s_{\mathrm{I},n_1}^2 s_{\mathrm{P},n_2}^2 \right). \tag{29}$$

Algorithm 3 M-SCA: IRS Phase Shift.

Input β_2, β_4, $\boldsymbol{h}_{\mathrm{D},n}$, $\boldsymbol{V}_n$, σ_n, $\boldsymbol{w}_{\mathrm{I/P},n}$, ρ, ϵ, $\forall n$
Construct $\boldsymbol{V}$, $\boldsymbol{M}$, $\boldsymbol{M}_n$, $\boldsymbol{C}_n$, $\boldsymbol{C}_{\mathrm{I/P},k}$, $\forall n,k$
Initialize $i \leftarrow 0$, $\boldsymbol{\Phi}^{(0)}$
If $\rho = 0$ **Then**
    Get $\boldsymbol{\Phi}^\star$ by maximizing (18) s.t. (25c), (25d)
Else
    Set $t_{\mathrm{I/P},k}^{(0)}$, $\forall k$ by (17)
    Compute $z^{(0)}$ by (19)
    Repeat
        $i \leftarrow i+1$
        Get $\boldsymbol{\Phi}^{(i)}$ by maximizing (24) s.t. (25c), (25d)
        Update $t_{\mathrm{I/P},k}^{(i)}$, $\forall k$ by (17)
        Compute $z^{(i)}$ by (19)
    Until $|z^{(i)} - z^{(i-1)}| \leq \epsilon$
    Set $\boldsymbol{\Phi}^\star = \boldsymbol{\Phi}^{(i)}$
End If
Get $\hat{\boldsymbol{\phi}}^\star$ by eigen decomposition, $\boldsymbol{\Phi}^\star = \hat{\boldsymbol{\phi}}^\star (\hat{\boldsymbol{\phi}}^\star)^H$
Set $\boldsymbol{\phi}^\star = e^{j\arg\left([\hat{\boldsymbol{\phi}}^\star]_{(1:L)} / [\hat{\boldsymbol{\phi}}^\star]_{(L+1)}\right)}$
Output $\boldsymbol{\phi}^\star$

Algorithm 4 BCD: Waveform, Beamforming and Splitting Ratio.

Input β_2, β_4, $\boldsymbol{h}_{\mathrm{D},n}$, $\boldsymbol{V}_n$, P, σ_n, $\bar{R}$, ϵ, $\forall n$
Initialize $i \leftarrow 0$, $\boldsymbol{\phi}^{(0)}$, $\boldsymbol{b}_{\mathrm{I/P},n}^{(0)}$, $\boldsymbol{s}_{\mathrm{I/P}}^{(0)}$, $\rho^{(0)}$, $\forall n$
Set $\boldsymbol{w}_{\mathrm{I/P},n}^{(0)}$, $\forall n$ by (26)
Compute $z^{(0)}$ by (29)
Repeat
    $i \leftarrow i+1$
    Get $\boldsymbol{\phi}^{(i)}$ based on $\boldsymbol{w}_{\mathrm{I/P}}^{(i-1)}$, $\rho^{(i-1)}$ by Algorithm 1
    Update $\boldsymbol{h}_n^{(i)}$, $\boldsymbol{b}_n^{(i)}$, $\forall n$ by (5), (27)
    Get $\boldsymbol{s}_{\mathrm{I/P}}^{(i)}$, $\rho^{(i)}$ by Algorithm 2
    Update $\boldsymbol{w}_{\mathrm{I/P},n}^{(i)}$, $\forall n$ by (26)
    Compute $z^{(i)}$ by (29)
Until $|z^{(i)} - z^{(i-1)}| \leq \epsilon$
Set $\boldsymbol{\phi}^\star = \boldsymbol{\phi}^{(i)}$, $\boldsymbol{w}_{\mathrm{I/P}}^\star = \boldsymbol{w}_{\mathrm{I/P}}^{(i)}$, $\rho^\star = \rho^{(i)}$
Output $\boldsymbol{\phi}^\star$, $\boldsymbol{w}_{\mathrm{I}}^\star$, $\boldsymbol{w}_{\mathrm{P}}^\star$, $\rho^\star$

constraints. Given a solution accuracy ϵ_{IPM} for the interior-point method, the computational complexity of Algorithm 3 is $\mathcal{O}\left(I_{\mathrm{M-SCA}}(L+1)^{4.5}\log(\epsilon_{\mathrm{IPM}}^{-1})\right)$, where $I_{\mathrm{M-SCA}}$ denotes the number of M-SCA iterations [43]. Note that $I_{\mathrm{M-SCA}} = 1$ for the WIT point since no current expression thus no SCA is involved.

E. Block Coordinate Descent

Based on the direct and cascaded CSIT, we iteratively update the passive beamforming $\boldsymbol{\phi}$ by Algorithm 1, the active precoder $\boldsymbol{b}_{\mathrm{I/P},n}$, $\forall n$ by equation (27), and the waveform amplitude $\boldsymbol{s}_{\mathrm{I/P}}$ and splitting ratio ρ by Algorithm 2, until convergence. The steps are summarized in the BCD Algorithm 4, whose computational complexity is exponential as inherited from Algorithm 2.

Proposition 5. *For any feasible initial point, the BCD Algorithm 4 is guaranteed to converge.*

Algorithm 5 LC-BCD: Waveform and Beamforming.

Input β_2, β_4, $\boldsymbol{h}_{\mathrm{D},n}$, $\boldsymbol{V}_n$, P, σ_n, δ, ρ, ϵ, $\forall n$
Initialize $i \leftarrow 0$, $\boldsymbol{\phi}^{(0)}$, $\boldsymbol{b}_{\mathrm{I/P},n}^{(0)}$, $\boldsymbol{s}_{\mathrm{I/P}}^{(0)}$, $\forall n$
Set $\boldsymbol{w}_{\mathrm{I/P},n}^{(0)}$, $\forall n$ by (26)
Compute $R^{(0)}$, $z^{(0)}$ by (28), (29)
Repeat
    $i \leftarrow i+1$
    Get $\boldsymbol{\phi}^{(i)}$ based on $\boldsymbol{w}_{\mathrm{I/P}}^{(i-1)}$ by Algorithm 3
    Update $\boldsymbol{h}_n^{(i)}$, $\boldsymbol{b}_n^{(i)}$, $\forall n$ by (5), (27)
    Update $\boldsymbol{s}_{\mathrm{I}}^{(i)}$, $\boldsymbol{s}_{\mathrm{P}}^{(i)}$ by (39), (40)
    Update $\boldsymbol{w}_{\mathrm{I/P},n}^{(i)}$, $\forall n$ by (26)
    Compute $R^{(i)}$, $z^{(i)}$ by (28), (29)
    If $\rho = 0$ **Then**
        $\Delta = R^{(i)} - R^{(i-1)}$
    Else
        $\Delta = z^{(i)} - z^{(i-1)}$
    End If
Until $|\Delta| \leq \epsilon$
Set $\boldsymbol{\phi}^\star = \boldsymbol{\phi}^{(i)}$, $\boldsymbol{w}_{\mathrm{I/P}}^\star = \boldsymbol{w}_{\mathrm{I/P}}^{(i)}$
Output $\boldsymbol{\phi}^\star$, $\boldsymbol{w}_{\mathrm{I}}^\star$, $\boldsymbol{w}_{\mathrm{P}}^\star$

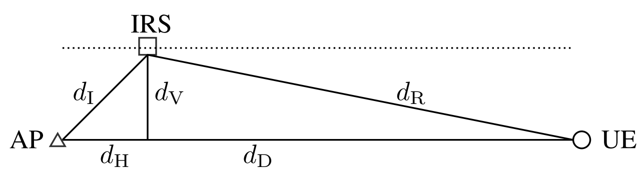

Fig. 5. System layout in simulation.

Proof. Please refer to Appendix D □

For the low-complexity design, when the receiver works in PS mode, we instead obtain the phase shift by Algorithm 3 and the waveform amplitude by (39) and (40). In contrast to the BCD algorithm that obtains the R-E region by varying the rate constraint from maximum capacity $C_{\max}$[8] to 0, the LC-BCD algorithm intends to draw the R-E tradeoff by performing a two-dimensional search that adjusts δ and ρ from 1 to 0. For the WIT point, $C_{\max}$ can be obtained as a special case of LC-BCD algorithm where $\rho = 0$ and the objective function becomes R instead of z. The steps are summarized in the Low Complexity-BCD (LC-BCD) Algorithm 5. Given a solution accuracy ϵ_{IPM} for the interior-point method, the computational complexity of Algorithm 5 is $\mathcal{O}\left(I_{\mathrm{LC-BCD}} I_{\mathrm{M-SCA}}(L+1)^{4.5}\log(\epsilon_{\mathrm{IPM}}^{-1})\right)$, where $I_{\mathrm{LC-BCD}}$ denotes the number of LC-BCD iterations [43].

IV. Performance Evaluations

To evaluate the performance of the proposed IRS-aided SWIPT system, we consider the layout in Fig. 5 where the IRS moves along a line parallel to the AP-UE path. Let d_{H}, d_{V} be the horizontal and vertical distances from the AP to the IRS, and denote respectively d_{D}, $d_{\mathrm{I}} = \sqrt{d_{\mathrm{H}}^2 + d_{\mathrm{V}}^2}$, $d_{\mathrm{R}} = \sqrt{(d_{\mathrm{D}} - d_{\mathrm{H}})^2 + d_{\mathrm{V}}^2}$ as the distance of direct, incident and reflected links. $d_{\mathrm{D}} = 12\mathrm{m}$ and $d_{\mathrm{H}} = d_{\mathrm{V}} = 2\mathrm{m}$ are chosen as

[8]Recall in Remark 2 that passive beamforming enables a resource allocation opportunity at the channel such that different capacities are achievable.

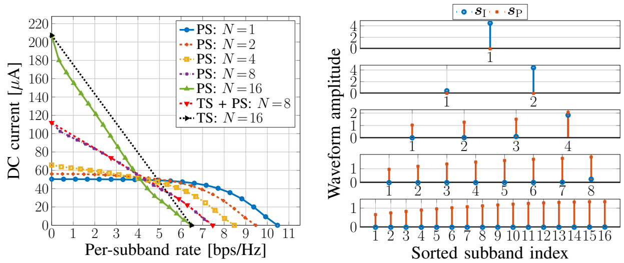

(a) R-E region (b) WPT waveform amplitude

Fig. 6. Average R-E region and WPT waveform amplitude versus N for $M=1$, $L=20$, $\sigma_n^2=-40$dBm, $B=1$MHz and $d_{\mathrm{H}}=d_{\mathrm{V}}=2$m.

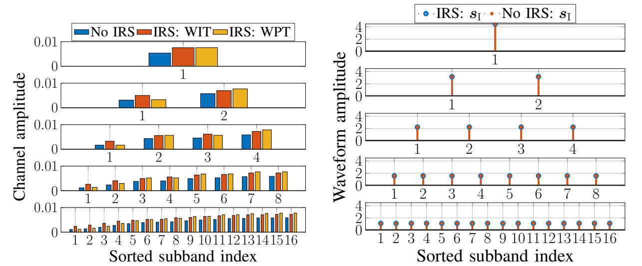

(a) Channel (b) WIT: modulated

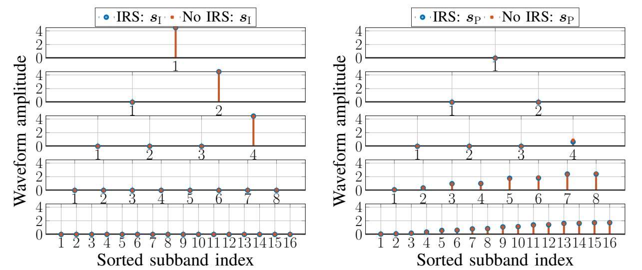

(c) WPT: modulated (d) WPT: multisine

Fig. 7. Sorted channel and waveform amplitude for WIT and WPT with and without IRS versus N for $M=1$, $L=100$, $\sigma_n^2=-40$dBm, $B=10$MHz and $d_{\mathrm{H}}=d_{\mathrm{V}}=2$m.

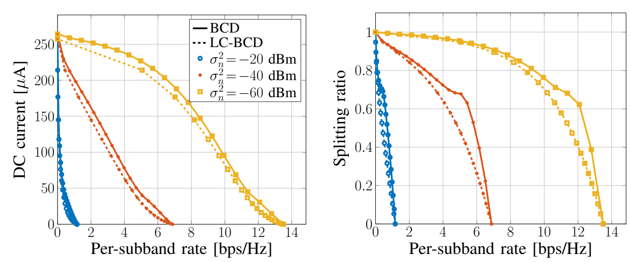

(a) R-E region (b) Splitting ratio

Fig. 8. Average R-E region and Splitting ratio versus σ_n^2 for $M=1$, $N=16$, $L=20$, $B=1$MHz and $d_{\mathrm{H}}=d_{\mathrm{V}}=2$m.

reference. The path loss of direct, incident and reflected links are denoted by Λ_{D}, Λ_{I} and Λ_{R}, respectively. We consider a large open space Wi-Fi-like environment at 2.4 GHz center frequency where the channel is modeled by IEEE TGn channel model D [48]. Specifically, the path loss exponent is set to 2 (i.e., free-space model) up to a breakpoint distance of 10 m, and set to 3.5 onwards. All fadings are modeled as Non-Line-of-Sight (NLoS) with tap delays and powers specified by model D. The tap gains are modeled as i.i.d. CSCG variables. Rectenna parameters are set to $k_2=0.0034$, $k_4=0.3829$, $R_{\mathrm{A}}=50\Omega$ such that $\beta_2=0.17$ and $\beta_4=957.25$ [8]. We also choose the average Effective Isotropic Radiated Power (EIRP) as $P=40$dBm, the receive antenna gain as 3 dBi, the scaling ratio as $\alpha=2$, the tolerance as $\epsilon=10^{-8}$, and assume $\delta=\rho$ for simplicity (hence one-dimensional search to obtain the R-E region). Each R-E region is averaged over 300 channel realizations, and the x-axis is normalized to per-subband rate R/N.

Fig. 6(a) illustrates the average R-E region versus the number of subband N. *First,* it is observed that increasing N reduces the per-subband rate but boosts the harvested energy. It is because less power is allocated to each subband but more balanced DC terms are introduced to boost the harvested energy. On the other hand, Fig. 6(b) sorts the modulated/multisine amplitude $\boldsymbol{s}_{\mathrm{I/P}}$ for WPT in descending order. It demonstrates that a dedicated multisine waveform is unnecessary for a small N but is required for a large N. This observation origins from the rectifier nonlinearity. Although both waveforms have equivalent second-order DC terms (10) and (12), for the fourth-order terms (11) and (13), the modulated waveform has N^2 monomials with a modulation gain of 2 while the multisine has $(2N^3+N)/3$ monomials. Hence, the benefit of multisine outstands for a sufficiently large N. *Second,* the R-E region is convex for $N\in\{2,4\}$ and concave-convex for $N\in\{8,16\}$. This has the consequence that PS outperforms TS for a small N and is outperformed for a large N. When N is in between, the optimal strategy is a combination of both, i.e., a time sharing between the WPT point and the saddle SWIPT point obtained by PS (as the red curve in Fig. 6(a)). For a relatively small N, the modulated waveform is used at both WIT and WPT point, and one can heuristically infer that no multisine waveform is needed for any R-E point (this is verified in simulation). In this case, the R-E region is convex, which aligns with the conventional linear harvester model (PS outperforms TS and dedicated power waveform is unnecessary). However, as N becomes sufficiently large, multisine waveform further boosts the WPT point and creates some concavity in the high-power region, which accounts for the superiority of TS under nonlinear harvester model. In conclusion, the rectifier nonlinearity enlarges the R-E region by favoring a different waveform and receiving mode, both heavily depend on the number of subbands. *Third,* the LC-BCD algorithm achieves a very good R-E performance even if one-dimensional search is considered for $\delta=\rho$ over [0,1]. This conclusion is also verified in the following plots.

The average noise power influences the R-E region as in Fig. 8(a). *First,* we note that the R-E region is roughly concave/convex at low/high SNR such that TS/PS are preferred correspondingly. At low SNR, the power is allocated to the modulated waveform on few strongest subbands to achieve a high rate. As the rate constraint $\bar{R}$ decreases, Algorithm 2 activates more subbands that further boosts the harvested DC power due to frequency coupling and harvester nonlinearity. *Second,* there exists a turning point in the R-E region especially for a low noise level ($\sigma_n^2\leq-40$dBm). The reason is that when $\bar{R}$ departs slightly from the maximum value, the algorithm tends

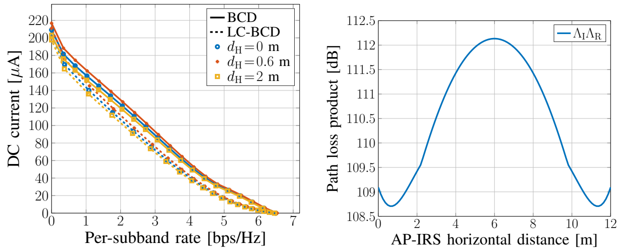

(a) R-E region (b) Path loss product

Fig. 9. Average R-E region and path loss versus $d_{\rm H}$ for $M=1$, $N=16$, $L=20$, $\sigma_n^2=-40$dBm, $B=1$MHz and $d_{\rm V}=2$m.

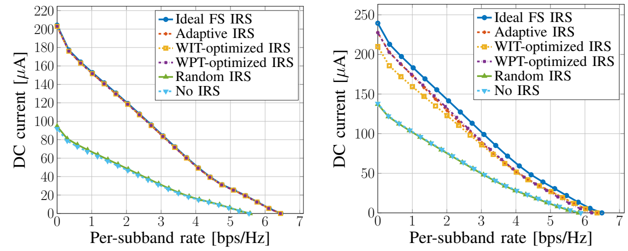

(a) $B=1$MHz (b) $B=10$MHz

Fig. 12. Average R-E region for ideal, adaptive, fixed and no IRS versus B for $M=1$, $N=16$, $L=20$, $\sigma_n^2=-40$dBm and $d_{\rm H}=d_{\rm V}=2$m.

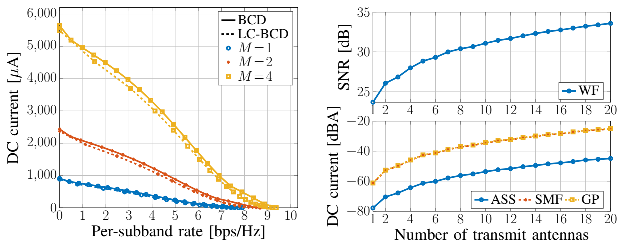

(a) R-E region (b) WIT SNR and WPT DC current

Fig. 10. Average R-E region, WIT SNR and WPT DC current versus M for $N=16$, $L=20$, $\sigma_n^2=-40$dBm, $B=1$MHz, $d_{\rm H}=d_{\rm V}=0.5$m.

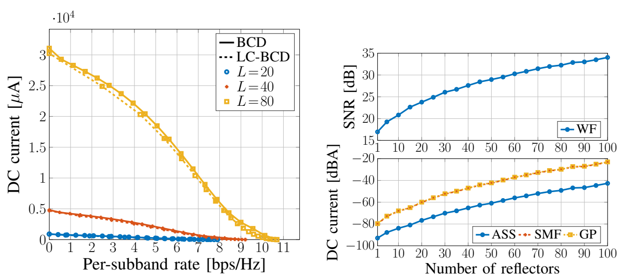

(a) R-E region (b) WIT SNR and WPT DC current

Fig. 11. Average R-E region, WIT SNR and WPT DC current versus L for $M=1$, $N=16$, $\sigma_n^2=-40$dBm, $B=1$MHz and $d_{\rm H}=d_{\rm V}=0.5$m.

to adjust the splitting ratio ρ rather than allocate more power to the multisine waveform, since a small amplitude multisine could be inefficient for energy purpose. As $\bar{R}$ further decreases, due to the advantage of multisine, a superposed waveform with a small ρ can outperform a modulated waveform with a large ρ. The result proves the benefit of superposed waveform and the necessity of joint waveform and splitting ratio optimization.

In Fig. 9(a), we compare the average R-E region achieved by different AP-IRS horizontal distance $d_{\rm H}$. Different from the active Amplify-and-Forward (AF) relay that favors midpoint development [49], the IRS should be placed close to either the AP or the UE based on the product path loss model that applies to finite-size element reflection [50], [51]. Moreover, there exist two optimal IRS coordinates around $d_{\rm H}=0.6$ and 11.4 m that minimize the path loss product $\Lambda_{\rm I}\Lambda_R$ thus maximize the R-E tradeoff. It suggests that equipping the AP with an IRS can potentially extend the operation range of SWIPT systems. Considering the passive characteristic of the IRS, chances are that it can be directly supported by the SWIPT network.

The impacts of the number of transmit antennas M and the IRS elements L on the R-E behavior are revealed in Figs. 10(a) and 11(a). *First,* adding either active or passive elements enhances the equivalent channel strength and boosts both information and power transfer, but has negligible influence on the optimal receiving strategy. *Second,* the conventional Linear Energy Harvester (LEH) model leads to power-inefficient design. To show the underlying performance loss, we truncate the DC objective function (8) at $n_0=2$ such that, 1) in the passive beamforming problem, $z(\mathbf{\Phi})=\beta_2\rho(t_{\rm I,0}+t_{\rm P,0})/2$ and no SCA is required, 2) in the waveform design problem, the WPT-optimal strategy is the Adaptive Single Sinewave (ASS) waveform strategy that allocates all power to the multisine at the strongest subband [8]. As shown in Figs. 10(b) and 11(b), those conventional designs do not exploit the harvester nonlinearity and end up with a nearly $20\,$dB current gap compared to the nonlinear model-based SMF and GP. *Third,* passive beamforming has a larger array gain and power scaling order than active beamforming. This behavior is more obvious for the case of WIT and WPT. For active beamforming, doubling M brings a $3\,$dB gain at the output SNR, which corresponds to a transmit array gain of M [47] and a doubled harvester input power. Thanks to the rectenna nonlinearity, the output DC current ends up with a nearly four-time ($12\,$dB) increase, which aligns with the active scaling law in the order of M^2 [14]. On the other hand, when the IRS is very close to the AP, doubling L increases the output SNR up to $6\,$dB, which implies a reflect array gain of L^2 [23]. An interpretation is that the IRS coherently combines the incoming signal with a receive array gain L, then performs an equal gain reflection with a transmit array gain L. Hence, doubling the number of IRS elements brings a four-fold increase on the received signal power that further amplifies the harvested DC current by 16 times ($24\,$dB), corresponding to a passive scaling law in the order of L^4. Compared with active antennas, IRS elements achieve higher array gain and power scaling order, but a very large L is required to compensate the double fading of the auxiliary link. These observations demonstrate the R-E benefit of passive beamforming and emphasize the importance of accounting for the harvester nonlinearity in the passive beamforming design.

Figs. 12(a) and 12(b) explore the R-E region with different IRS strategies for narrowband and broadband SWIPT. The ideal Frequency-Selective (FS) IRS assumes the reflection coefficient of each element is independent and controllable at different frequencies. The adaptive IRS adjusts the passive beamforming for

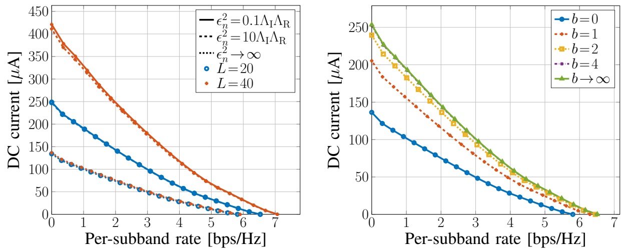

(a) Imperfect cascaded CSIT (b) Quantized IRS

Fig. 13. Average R-E region with imperfect cascaded CSIT and quantized IRS for $M=1$, $N=16$, $L=20$, $\sigma_n^2=-40\,\mathrm{dBm}$, $B=10\,\mathrm{MHz}$ and $d_{\mathrm{H}}=d_{\mathrm{V}}=2\mathrm{m}$. $\epsilon_n^2 \to \infty$ corresponds to no CSIT and random IRS; $b=0$ and $b \to \infty$ correspond respectively to no IRS and continuous IRS.

different R-E points by Algorithm 1. The WIT/WPT-optimized IRS is retrieved by Algorithm 3 then fixed for the whole R-E region. The random IRS models the phase shift of all elements as i.i.d. uniform random variables over $[0, 2\pi)$. *First,* random IRS and no IRS perform worse than other schemes since no passive beamforming is exploited. Their R-E boundaries coincide because the antenna mode reflection of the random IRS is canceled out after averaging over the channel realizations. *Second,* the performance of ideal, adaptive and WIT/WPT-optimized IRS are similar when the bandwidth is small, while the adaptive IRS outperforms the WIT/WPT-optimized IRS but is outperformed by the ideal FS IRS when the bandwidth is large. In the former case, the subband responses are close to each other such that the tradeoff in Remark 2 becomes insignificant, and the auxiliary link can be roughly maximized at all subbands. It suggests that for narrowband SWIPT, the optimal passive beamforming for any R-E point is optimal for the whole R-E region, and the corresponding composite channel and active precoder are also optimal for the whole R-E region. Hence, the achievable R-E region is obtained by varying the waveform amplitude and splitting ratio. On the other hand, since the channel frequency selectivity affects the performance of information decoder and energy harvester differently, the optimal IRS reflection coefficient varies at different R-E tradeoff points for broadband SWIPT. By adaptive passive beamforming, the equivalent channel strength can be either amplified at the few strongest subbands to enhance the rate at low SNR, or spread evenly to boost the output DC power. It emphasizes the R-E advantage of adaptive passive beamforming design for broadband SWIPT.

We then explore the impacts of imperfect cascaded CSIT and quantized IRS on the R-E performance. Due to the general lack of RF-chains at the IRS, it can be challenging to acquire accurate cascaded CSIT on a short-term basis. Consider an imperfect CSIT model where the estimation of the cascaded link at subband n is

$$\hat{\boldsymbol{V}}_n = \boldsymbol{V}_n + \tilde{\boldsymbol{V}}_n, \tag{41}$$

where $\tilde{\boldsymbol{V}}_n$ is the estimation error with entries following i.i.d. CSCG distribution $\mathcal{CN}(0, \epsilon_n^2)$. Perfect CSIT can be regarded as a special case with $\epsilon_n = 0$. Note that the estimations at different subbands are independent, but the subchannel responses are indeed correlated. Figure 13(a) shows that the proposed passive beamforming Algorithm 1 is robust to cascaded CSIT inaccuracy for broadband SWIPT with different L. On the other hand, since the practical reflection coefficient depends on the available element impedances, we consider a discrete uniform IRS codebook $\mathcal{C}_\phi = \{e^{j2\pi i/2^b} \mid i = 1, \ldots, 2^b\}$ and perform quantization on the continuous reflection coefficients returned by Algorithm 4 to reduce the circuit complexity and control overhead[9]. Figure 13(b) suggests that even $b=1$ (i.e., two-state reflection) brings considerable R-E gain over the benchmark scheme without IRS, and the performance gap between $b=4$ and unquantized IRS is negligible. These observations demonstrate the advantage of the proposed joint waveform, active and passive beamforming design in practical IRS-aided SWIPT systems.

V. Conclusion and Future Works

This paper investigated the R-E tradeoff of a single user employing practical receiving strategies in a novel IRS-aided multi-carrier MISO SWIPT system. Uniquely, we consider the joint waveform, active and passive beamforming design under rectifier nonlinearity to maximize the achievable R-E region. A three-stage BCD algorithm is proposed to solve the problem. In the first stage, the IRS phase shift is obtained by the SCA technique and eigen decomposition. In the second and third stages, the active precoder is derived in closed form, and the waveform amplitude and splitting ratio are optimized by the GP method. We also propose and combine closed-form adaptive waveform schemes with a modified passive beamforming strategy to formulate a low-complexity BCD algorithm that achieves decent performance in different scenarios. Numerical results reveal significant R-E gains by modeling harvester nonlinearity in the passive beamforming and entire IRS-aided SWIPT design. Compared with active antennas, IRS elements cannot be designed independently across frequencies, but can integrate coherent combining and equal gain transmission in a fully passive manner to boost the array gain and power scaling order. However, a large number of reflecting elements may be required to compensate the double fading in the auxiliary link.

One particular unanswered question of this paper is how to design waveform, active and passive beamforming in a multi-user multi-carrier IRS-aided SWIPT system. Also, the use of more involved IRS architecture based on direction- and frequency-dependent reflection [24] and/or partially/fully-connected reflection [53] could be considered in future works.

Appendix

A. Proof of Proposition 1

For any feasible $\boldsymbol{\Phi}$ to problem (25), $\mathrm{tr}(\boldsymbol{\Phi}) = L+1$ always holds due to the modulus constraint (25c). Therefore, we add

[9]Note that this relax-then-quantize approach can bring notable performance loss compared with direct optimization over the discrete phase shift set, especially for a small b (i.e., low-resolution IRS). The readers are referred to [52] for details.

a constant term $-\mathrm{tr}(\mathbf{\Phi})$ to (25a) and recast problem (25) as

$$\max_{\mathbf{\Phi}} \quad -\mathrm{tr}(\mathbf{\Phi})+\tilde{z}(\mathbf{\Phi}) \tag{42a}$$
$$\text{s.t.} \quad R(\mathbf{\Phi})\geq \bar{R}, \tag{42b}$$
$$\mathrm{diag}^{-1}(\mathbf{\Phi})=\mathbf{1}, \tag{42c}$$
$$\mathbf{\Phi}\succeq \mathbf{0}, \tag{42d}$$
$$\mathrm{rank}(\mathbf{\Phi})=1. \tag{42e}$$

By applying SDR, problem (42a)–(42d) is convex w.r.t. $\mathbf{\Phi}$ and satisfies the Slater's condition [54], thus strong duality holds. The corresponding Lagrangian function at iteration i is given by (43), where μ, $\boldsymbol{\nu}$, $\mathbf{\Upsilon}$ denote respectively the scalar, vector and matrix Lagrange multiplier associated with constraint (42b), (42c) and (42d), and ζ collects all terms irrelevant to $\mathbf{\Phi}^{(i)}$. The Karush–Kuhn–Tucker (KKT) conditions on the primal and dual solutions are

$$\mu^\star\geq 0,\mathbf{\Upsilon}^\star\succeq\mathbf{0}, \tag{44a}$$
$$\boldsymbol{\nu}^\star\odot\mathrm{diag}^{-1}(\mathbf{\Phi}^\star)=\mathbf{0},\mathbf{\Upsilon}^\star\mathbf{\Phi}^\star=\mathbf{0}, \tag{44b}$$
$$\nabla_{\mathbf{\Phi}^\star}\mathcal{L}=0. \tag{44c}$$

We then derive the gradient explicitly and rewrite (44c) as

$$\mathbf{\Upsilon}^\star=\boldsymbol{I}-\mathbf{\Delta}^\star, \tag{45}$$

where $\mathbf{\Delta}^\star$ is given by (46). Note that (44b) suggests $\mathrm{rank}(\mathbf{\Upsilon}^\star)+\mathrm{rank}(\mathbf{\Phi}^\star)\leq L+1$. By reusing the proof in Appendix A of [55], we conclude $\mathrm{rank}(\mathbf{\Upsilon}^\star)\geq L$. On the other hand, $\mathbf{\Phi}^\star$ cannot be zero matrix and $\mathrm{rank}(\mathbf{\Phi}^\star)\geq 1$. Therefore, any optimal solution $\mathbf{\Phi}^\star$ to the relaxed problem (42) is rank-1. Due to the equivalence between (25a) and (42a), $\mathbf{\Phi}^\star$ is also optimal to the relaxed problem (25) and Proposition 1 holds.

B. Proof of Proposition 2

The objective function (25a) is non-decreasing over iterations because the solution to (25a)–(25d) at iteration $i-1$ is still feasible at iteration i. Also, the sequence $\{\tilde{z}(\mathbf{\Phi}^{(i)})\}_{i=1}^{\infty}$ is bounded above due to the unit-modulus constraint (25c). Thus, Algorithm 1 is guaranteed to converge. Besides, we notice that Algorithm 1 is an inner approximation algorithm [56], because $\tilde{z}(\mathbf{\Phi})\leq z(\mathbf{\Phi})$, $\partial\tilde{z}(\mathbf{\Phi}^{(i)})/\partial\mathbf{\Phi}=\partial z(\mathbf{\Phi}^{(i)})/\partial\mathbf{\Phi}$ and the approximation (20)–(22) are asymptotically tight as $i\to\infty$ [57]. Therefore, it is guaranteed to provide a local optimal $\mathbf{\Phi}^\star$ to the relaxed passive beamforming problem. According to Proposition 1, $\mathbf{\Phi}^\star$ is rank-1 such that $\boldsymbol{\phi}^\star$ can be extracted without performance loss and the local optimality inherits to the original problem (15).

C. Proof of Proposition 3

From the perspective of WIT, the MRT precoder maximizes $|\boldsymbol{h}_n^H\boldsymbol{w}_{\mathrm{I},n}|=\|\boldsymbol{h}_n\|s_{\mathrm{I},n}$ thus maximizes the rate (7). From the perspective of WPT, the MRT precoder maximizes $(\boldsymbol{h}_n^H\boldsymbol{w}_{\mathrm{I/P},n})(\boldsymbol{h}_n^H\boldsymbol{w}_{\mathrm{I/P},n})^*=\|\boldsymbol{h}_n\|^2 s_{\mathrm{I/P},n}^2$ thus maximizes the second and fourth order DC terms (10)–(13). Therefore, MRT is the global optimal information and power precoder.

D. Proof of Proposition 5

The objective function (15a) is non-decreasing over the iterations, because the IRS phase shift by Algorithm 1 is local optimal, the active precoder by (27) is global optimal, and the waveform amplitude and splitting ratio by Algorithm 2 are local optimal. (15a) is also upper-bounded due to the unit-modulus constraint (15d) and the transmit power constraint (15c). Therefore, Algorithm 4 is guaranteed to converge. However, it may not converge to optimal points since variables are coupled in constraint (15b) [58].

References

[1] B. Clerckx, R. Zhang, R. Schober, D. W. K. Ng, D. I. Kim, and H. V. Poor, "Fundamentals of wireless information and power transfer: From rf energy harvester models to signal and system designs," *IEEE Journal on Selected Areas in Communications*, vol. 37, no. 1, pp. 4–33, Jan. 2019.

[2] L. R. Varshney, "Transporting information and energy simultaneously," in *2008 IEEE International Symposium on Information Theory*. IEEE, Jul. 2008, pp. 1612–1616.

[3] X. Zhou, R. Zhang, and C. K. Ho, "Wireless information and power transfer: Architecture design and rate-energy tradeoff," *IEEE Transactions on Communications*, vol. 61, no. 11, pp. 4754–4767, Nov. 2013.

$$\begin{aligned}\mathcal{L}=&\,\mathrm{tr}\Big(\mathbf{\Phi}^{(i)}\Big)-\frac{1}{2}\beta_2\rho\,\mathrm{tr}\Big((\boldsymbol{C}_{\mathrm{I},0}+\boldsymbol{C}_{\mathrm{P},0})\mathbf{\Phi}^{(i)}\Big)-\frac{3}{4}\beta_4\rho^2\Bigg(2t_{\mathrm{I},0}^{(i-1)}\mathrm{tr}\Big(\boldsymbol{C}_{\mathrm{I},0}\mathbf{\Phi}^{(i)}\Big)+\sum_{k=-N+1}^{N-1}(t_{\mathrm{P},k}^{(i-1)})^*\mathrm{tr}\Big(\boldsymbol{C}_{\mathrm{P},k}\mathbf{\Phi}^{(i)}\Big)\\&+2t_{\mathrm{P},0}^{(i-1)}\mathrm{tr}\Big(\boldsymbol{C}_{\mathrm{I},0}\mathbf{\Phi}^{(i)}\Big)+2t_{\mathrm{I},0}^{(i-1)}\mathrm{tr}\Big(\boldsymbol{C}_{\mathrm{P},0}\mathbf{\Phi}^{(i)}\Big)\Bigg)+\mu\Bigg(2^{\bar{R}}-\prod_{n=1}^{N}\Bigg(1+\frac{(1-\rho)\mathrm{tr}\Big(\boldsymbol{C}_n\mathbf{\Phi}^{(i)}\Big)}{\sigma_n^2}\Bigg)\Bigg)\\&+\mathrm{tr}\Big(\mathrm{diag}(\boldsymbol{\nu})\odot\Big(\mathbf{\Phi}^{(i)}\odot\boldsymbol{I}-\boldsymbol{I}\Big)\Big)-\mathrm{tr}\Big(\mathbf{\Upsilon}\mathbf{\Phi}^{(i)}\Big)+\zeta.\end{aligned} \tag{43}$$

$$\begin{aligned}\mathbf{\Delta}^\star=&\,\frac{1}{2}\beta_2\rho(\boldsymbol{C}_{\mathrm{I},0}+\boldsymbol{C}_{\mathrm{P},0})+\frac{3}{4}\beta_4\rho^2\Bigg(2t_{\mathrm{I},0}^{(i-1)}\boldsymbol{C}_{\mathrm{I},0}+\sum_{k=-N+1}^{N-1}(t_{\mathrm{P},k}^{(i-1)})^*\boldsymbol{C}_{\mathrm{P},k}+2t_{\mathrm{P},0}^{(i-1)}\boldsymbol{C}_{\mathrm{I},0}+2t_{\mathrm{I},0}^{(i-1)}\boldsymbol{C}_{\mathrm{P},0}\Bigg)\\&+\mu^\star\sum_{n=1}^{N}\frac{(1-\rho)\boldsymbol{C}_n}{\sigma_n^2}\prod_{n'=1,n'\neq n}^{N}\Bigg(1+\frac{(1-\rho)\mathrm{tr}\Big(\boldsymbol{C}_{n'}\mathbf{\Phi}^\star\Big)}{\sigma_{n'}^2}\Bigg)-\mathrm{diag}(\boldsymbol{\nu}^\star).\end{aligned} \tag{46}$$

[4] R. Zhang and C. K. Ho, "Mimo broadcasting for simultaneous wireless information and power transfer," *IEEE Transactions on Wireless Communications*, vol. 12, no. 5, pp. 1989–2001, May 2013.

[5] J. Park and B. Clerckx, "Joint wireless information and energy transfer in a k-user mimo interference channel," *IEEE Transactions on Wireless Communications*, vol. 13, no. 10, pp. 5781–5796, Oct. 2014.

[6] M. Trotter, J. Griffin, and G. Durgin, "Power-optimized waveforms for improving the range and reliability of rfid systems," in *2009 IEEE International Conference on RFID*. IEEE, Apr. 2009, pp. 80–87.

[7] B. Clerckx and J. Kim, "On the beneficial roles of fading and transmit diversity in wireless power transfer with nonlinear energy harvesting," *IEEE Transactions on Wireless Communications*, vol. 17, no. 11, pp. 7731–7743, Nov. 2018.

[8] B. Clerckx and E. Bayguzina, "Waveform design for wireless power transfer," *IEEE Transactions on Signal Processing*, vol. 64, no. 23, pp. 6313–6328, Dec. 2016.

[9] J. Kim, B. Clerckx, and P. D. Mitcheson, "Experimental analysis of harvested energy and throughput trade-off in a realistic swipt system," in *2019 IEEE Wireless Power Transfer Conference (WPTC)*. IEEE, Jun. 2019, pp. 1–5.

[10] ——, "Signal and system design for wireless power transfer: Prototype, experiment and validation," *IEEE Transactions on Wireless Communications*, vol. 19, no. 11, pp. 7453–7469, Nov. 2020.

[11] J. Kim and B. Clerckx, "Range expansion for wireless power transfer using joint beamforming and waveform architecture: An experimental study in indoor environment," *IEEE Wireless Communications Letters*, vol. 2337, no. 1, pp. 1–5, 2021.

[12] B. Clerckx and E. Bayguzina, "Low-complexity adaptive multisine waveform design for wireless power transfer," *IEEE Antennas and Wireless Propagation Letters*, vol. 16, no. 1, pp. 2207–2210, 2017.

[13] J. Kim, B. Clerckx, and P. D. Mitcheson, "Prototyping and experimentation of a closed-loop wireless power transmission with channel acquisition and waveform optimization," in *2017 IEEE Wireless Power Transfer Conference (WPTC)*. IEEE, May 2017, pp. 1–4.

[14] B. Clerckx, "Wireless information and power transfer: Nonlinearity, waveform design, and rate-energy tradeoff," *IEEE Transactions on Signal Processing*, vol. 66, no. 4, pp. 847–862, Feb. 2018.

[15] M. Varasteh, B. Rassouli, and B. Clerckx, "On capacity-achieving distributions for complex awgn channels under nonlinear power constraints and their applications to swipt," *IEEE Transactions on Information Theory*, vol. 66, no. 10, pp. 6488–6508, Oct. 2020.

[16] ——, "Swipt signaling over frequency-selective channels with a nonlinear energy harvester: Non-zero mean and asymmetric inputs," *IEEE Transactions on Communications*, vol. 67, no. 10, pp. 7195–7210, Oct. 2019.

[17] M. Varasteh, J. Hoydis, and B. Clerckx, "Learning to communicate and energize: Modulation, coding, and multiple access designs for wireless information-power transmission," *IEEE Transactions on Communications*, vol. 68, no. 11, pp. 6822–6839, Nov. 2020.

[18] R. Anwar, L. Mao, and H. Ning, "Frequency selective surfaces: A review," *Applied Sciences*, vol. 8, no. 9, p. 1689, Sep. 2018.

[19] T. J. Cui, M. Q. Qi, X. Wan, J. Zhao, and Q. Cheng, "Coding metamaterials, digital metamaterials and programmable metamaterials," *Light: Science & Applications*, vol. 3, no. 10, pp. e218–e218, Oct. 2014.

[20] C. Liaskos, S. Nie, A. Tsioliaridou, A. Pitsillides, S. Ioannidis, and I. Akyildiz, "Realizing wireless communication through software-defined hypersurface environments," in *2018 IEEE 19th International Symposium on "A World of Wireless, Mobile and Multimedia Networks" (WoWMoM)*. IEEE, Jun. 2018, pp. 14–15.

[21] Q. Wu and R. Zhang, "Intelligent reflecting surface enhanced wireless network: Joint active and passive beamforming design," in *2018 IEEE Global Communications Conference (GLOBECOM)*, vol. 18, no. 11. IEEE, Dec. 2018, pp. 1–6.

[22] ——, "Beamforming optimization for intelligent reflecting surface with discrete phase shifts," in *ICASSP 2019 - 2019 IEEE International Conference on Acoustics, Speech and Signal Processing (ICASSP)*. IEEE, May 2019, pp. 7830–7833.

[23] ——, "Intelligent reflecting surface enhanced wireless network via joint active and passive beamforming," *IEEE Transactions on Wireless Communications*, vol. 18, no. 11, pp. 5394–5409, Nov. 2019.

[24] S. Abeywickrama, R. Zhang, and C. Yuen, "Intelligent reflecting surface: Practical phase shift model and beamforming optimization," in *ICC 2020 - 2020 IEEE International Conference on Communications (ICC)*. IEEE, Jun. 2020, pp. 1–6.

[25] Q.-U.-A. Nadeem, A. Kammoun, A. Chaaban, M. Debbah, and M.-S. Alouini, "Intelligent reflecting surface assisted wireless communication: Modeling and channel estimation," *arXiv preprint arXiv:1906.02360*, pp. 1–7, 2019.

[26] C. You, B. Zheng, and R. Zhang, "Intelligent reflecting surface with discrete phase shifts: Channel estimation and passive beamforming," in *ICC 2020 - 2020 IEEE International Conference on Communications (ICC)*. IEEE, Jun. 2020, pp. 1–6.

[27] J.-M. Kang, "Intelligent reflecting surface: Joint optimal training sequence and refection pattern," *IEEE Communications Letters*, vol. 24, no. 8, pp. 1784–1788, Aug. 2020.

[28] P. Wang, J. Fang, H. Duan, and H. Li, "Compressed channel estimation for intelligent reflecting surface-assisted millimeter wave systems," *IEEE Signal Processing Letters*, vol. 27, pp. 905–909, 2020.

[29] Q. Wu and R. Zhang, "Towards smart and reconfigurable environment: Intelligent reflecting surface aided wireless network," *IEEE Communications Magazine*, vol. 58, no. 1, pp. 106–112, Jan. 2020.

[30] Y. Yang, S. Zhang, and R. Zhang, "Irs-enhanced ofdma: Joint resource allocation and passive beamforming optimization," *IEEE Wireless Communications Letters*, vol. 9, no. 6, pp. 760–764, Jun. 2020.

[31] L. Dai, M. D. Renzo, C. B. Chae, L. Hanzo, B. Wang, M. Wang, X. Yang, J. Tan, S. Bi, S. Xu, F. Yang, and Z. Chen, "Reconfigurable intelligent surface-based wireless communications: Antenna design, prototyping, and experimental results," *IEEE Access*, vol. 8, pp. 45 913–45 923, 2020.

[32] H. Yang, Z. Xiong, J. Zhao, D. Niyato, L. Xiao, and Q. Wu, "Deep reinforcement learning-based intelligent reflecting surface for secure wireless communications," *IEEE Transactions on Wireless Communications*, vol. 20, no. 1, pp. 375–388, 2021.

[33] Q. Wu and R. Zhang, "Weighted sum power maximization for intelligent reflecting surface aided swipt," *IEEE Wireless Communications Letters*, vol. 9, no. 5, pp. 586–590, May 2020.

[34] Y. Tang, G. Ma, H. Xie, J. Xu, and X. Han, "Joint transmit and reflective beamforming design for irs-assisted multiuser miso swipt systems," in *ICC 2020 - 2020 IEEE International Conference on Communications (ICC)*. IEEE, Jun. 2020, pp. 1–6.

[35] Q. Wu and R. Zhang, "Joint active and passive beamforming optimization for intelligent reflecting surface assisted swipt under qos constraints," *IEEE Journal on Selected Areas in Communications*, vol. 38, no. 8, pp. 1735–1748, Aug. 2020.

[36] D. Xu, V. Jamali, X. Yu, D. W. K. Ng, and R. Schober, "Optimal resource allocation design for large irs-assisted swipt systems: A scalable optimization framework," *arXiv preprint arXiv:2104.03346*, pp. 1–30, 2021.

[37] Q. Wu, X. Guan, and R. Zhang, "Intelligent reflecting surface aided wireless energy and information transmission: An overview," *arXiv preprint arXiv:2106.07997*, pp. 1–39, Jun. 2021.

[38] R. Hansen, "Relationships between antennas as scatterers and as radiators," *Proceedings of the IEEE*, vol. 77, no. 5, pp. 659–662, May 1989.

[39] B. Clerckx, K. Huang, L. R. Varshney, S. Ulukus, and M.-S. Alouini, "Wireless power transfer for future networks: Signal processing, machine learning, computing, and sensing," *arXiv preprint arXiv:2101.04810*, pp. 1–33, 2021.

[40] M. Pinuela, P. D. Mitcheson, and S. Lucyszyn, "Ambient rf energy harvesting in urban and semi-urban environments," *IEEE Transactions on Microwave Theory and Techniques*, vol. 61, no. 7, pp. 2715–2726, Jul. 2013.

[41] T. Adali and S. Haykin, *Adaptive Signal Processing*, T. Adali and S. Haykin, Eds. Hoboken, NJ, USA: John Wiley & Sons, Mar. 2010.

[42] Y. Huang and B. Clerckx, "Large-scale multiantenna multisine wireless power transfer," *IEEE Transactions on Signal Processing*, vol. 65, no. 21, pp. 5812–5827, Nov. 2017.

[43] Z.-q. Luo, W.-k. Ma, A. So, Y. Ye, and S. Zhang, "Semidefinite relaxation of quadratic optimization problems," *IEEE Signal Processing Magazine*, vol. 27, no. 3, pp. 20–34, May 2010.

[44] M. Grant, S. Boyd, and Y. Ye, "Cvx: Matlab software for disciplined convex programming," 2008.

[45] S. Boyd, S.-J. Kim, L. Vandenberghe, and A. Hassibi, "A tutorial on geometric programming," *Optimization and Engineering*, vol. 8, no. 1, pp. 67–127, May 2007.

[46] M. Chiang, *Geometric Programming for Communication Systems*. now Publishers Inc, 2005, vol. 2, no. 1.

[47] D. Tse and P. Viswanath, *Fundamentals of Wireless Communication*. Cambridge University Press, May 2005, vol. 9780521845.

[48] V. Erceg, "Tgn channel models," in *IEEE 802.11-03/940r4*, 2004.

[49] S. Li, K. Yang, M. Zhou, J. Wu, L. Song, Y. Li, and H. Li, "Full-duplex amplify-and-forward relaying: Power and location optimization," *IEEE Transactions on Vehicular Technology*, vol. 66, no. 9, pp. 8458–8468, Sep. 2017.

[50] O. Ozdogan, E. Bjornson, and E. G. Larsson, "Intelligent reflecting surfaces: Physics, propagation, and pathloss modeling," *IEEE Wireless Communications Letters*, vol. 9, no. 5, pp. 581–585, May 2020.

[51] W. Tang, M. Z. Chen, X. Chen, J. Y. Dai, Y. Han, M. Di Renzo, Y. Zeng, S. Jin, Q. Cheng, and T. J. Cui, "Wireless communications with reconfigurable intelligent surface: Path loss modeling and experimental measurement," *IEEE Transactions on Wireless Communications*, vol. 20, no. 1, pp. 421–439, Jan. 2021.

[52] Q. Wu and R. Zhang, "Beamforming optimization for wireless network aided by intelligent reflecting surface with discrete phase shifts," *IEEE Transactions on Communications*, vol. 68, no. 3, pp. 1838–1851, Mar. 2020.

[53] S. Shen, B. Clerckx, and R. Murch, "Modeling and architecture design of intelligent reflecting surfaces using scattering parameter network analysis," *arXiv preprint arXiv:2011.11362*, pp. 1–30, Nov. 2020.

[54] S. Boyd and L. Vandenberghe, *Convex Optimization*. Cambridge University Press, Mar. 2004.

[55] D. Xu, X. Yu, Y. Sun, D. W. K. Ng, and R. Schober, "Resource allocation for irs-assisted full-duplex cognitive radio systems," *IEEE Transactions on Communications*, vol. 68, no. 12, pp. 7376–7394, Dec. 2020.

[56] B. R. Marks and G. P. Wright, "A general inner approximation algorithm for nonconvex mathematical programs," *Operations Research*, vol. 26, no. 4, pp. 681–683, Aug. 1978.

[57] W.-C. Li, T.-H. Chang, C. Lin, and C.-Y. Chi, "Coordinated beamforming for multiuser miso interference channel under rate outage constraints," *IEEE Transactions on Signal Processing*, vol. 61, no. 5, pp. 1087–1103, Mar. 2013.

[58] L. Grippo and M. Sciandrone, "On the convergence of the block nonlinear gauss–seidel method under convex constraints," *Operations Research Letters*, vol. 26, no. 3, pp. 127–136, Apr. 2000.